Computing the Aeroelastic Disk Vibrations in a Hard Disk Drive

Sujit Kirpekar and David B. Bogy

Computer Mechanics Laboratory

Department of Mechanical Engineering

University of California at Berkeley

Berkeley, CA 94720

Telephone: (510)642-4975

Fax: (510)643-9786

kirpekar@newton.berkeley.edu

January 5, 2006

Contents

List of Figures

List of Tables

Abstract

In this report, the turbulent flow of air caused by the spinning of a single disk inside a typical hard disk drive casing is calculated using large eddy simulation (LES). The pressure acting on the disk is recorded as a function of time and is used to compute the vibrations of the spinning disk using a self-developed hybrid spectral-finite difference code. Two commonly occurring cases are compared and contrasted: a disk actuated on one side only and a disk actuated on both sides. The pressure loading on the disk is characterized in terms of its mean, root-mean-square (RMS) and its spectral content. After comprehensive verification and validation of the code it is used to compute the disk vibrations for these two cases, which show very different vibration responses. Additional insights about the flow are also developed by analyzing the velocity field generated by the disks, the flow in the shroud gap and some global integral quantities of the flow.

1 Introduction

The rotating disk is the principal mechanical component of a hard disk drive. The dynamic stability of the disk in its transverse motion is of great importance to the successful operation of the hard drive. Over the years, the need for faster data transfer rates has lead to an increase in rotational speeds of disk drives. To counter the adverse effects of high speed rotation, disks have generally grown thicker, increasing their inertia and stiffness. However, the dynamic stability of the disk itself is not the only concern. Read-write heads in modern hard disk drives are positioned only a few nanometers adjacent to these rotating disks, by means of air bearing sliders. Due to the non-linear coupled nature of the head-disk interface transverse vibrations of the disk may cause significant sideways motions ("off track" motions) of the slider-head. Such off track motions are detrimental to the accurate positioning of the read-write head on data tracks. In more extreme situations, disk vibrations may lead to the slider

crashing on the disk, which results from a breakdown of the air bearing, possibily damaging the disk and/or the slider and contaminating the drive with wear particles.

Increasing spindle motor speeds have also led to the possibility of disks achieving their critical speed, which is the minimum rotational speed at which the backward traveling waves become standing waves on the disk. Due to the stationary forcing of the air bearing slider, such standing waves quickly become resonant, leading to high amplitude vibrations of the disk. Experimental data shows that current disk drives operate at approximately 40-50% of their critical speeds, but increasing drive RPMs and the need for thinner disks may bring such disks closer to the critical resonance. Disks which operate in the supercritical speed regime (e.g. floppy disks which are designed to do so) have the additional risk of undergoing hydrodynamically coupled resonant vibrations called "flutter". While this is not a concern for thicker and stiffer hard disks, the air flow results that we present may also be used as a model to simulate the aeroelastic vibrations of floppy disks.

1.1 Prior Work

The vibrations and stability of a spinning disk have been studied for almost a century now. There have been significant advances both in the fluid mechanics of flows surrounding spinning disks and the structural vibrations induced by such flows. A number of authors have studied the aeroelastic stability (stability to self-excited vibrations) of spinning disks. For a summary of this research, see references [1] to [12] in Kang and Raman (2004). Some investigations have used unenclosed rotating disks, while others have used more realistic enclosed rotating disks. Most of the efforts, however, have used either ad-hoc rotating damping operators to model the surrounding flow or hydrodynamic lubrication theory to model the coupling of the flow with the disk. Generally, such models based on compressible potential flow are suitable for floppy disks or circular saws, where the air film thickness is small. In hard disk drives, in addition to a large air film thickness (2-3 times the thickness

of the disk), the azimuthal symmetry of the flow is broken by the presence of the actuator. This obstruction causes rapid unsteady motions in the wake its sheds. The turbulent wake is transported (and dissipated) with the rotating disks and comes around to flow over the obstruction again. It is unlikely for such a complicated turbulent flow to be ever described by an analytical model. Moreover, given the complicated and frequently changing design of actuator components (such as the suspension), the only feasible method to compute realistic disk vibrations would be to solve for the flow in a separate CFD calculation and use the pressure and shear data to compute the disk vibrations.

For commercially available hard drives, experimental results suggest (Fukaya et al., 2002) that the vibrations of the disk are independent of the instability of the flow. Moreover, in typical hard disk drives, the experimentally measured vibrations of disks (due to all sources) are less than 0.1% of the width of the entire hard drive enclosure and the maximum linear speed of disks is approximately 10% of the acoustic speed in air. All this implies that compressible effects of the flow may be small, while the turbulence induced effects on the disk vibration may be larger.

In general, accurate information about disk vibrations computed using CFD based air pressure data is lacking.

Tatewaki et al. (2001) provides LES results of the a coupled CFD-structural calculation in which they report the vibrations of the disk with and without a simplified obstruction. Yuan et al. (2004) computed the flow in a deformed disk enclosed inside a casing, but with an open shroud. They present results for the pressure and shear forces on the disk in its deformed umbrella-like shape as a function of the Reynolds number. Unfortunately, their model did not have any obstruction (e.g. an actuator) and hence resulted in a completely different flow field from what is encountered in a disk drive. Also, the deflection of the disk was unreasonably large: 25% of the width of the entire hard drive enclosure, while it is typically of the order of 0.1%.

Imai (2001), Chang et al. (2002) and Guo and Chen (2001), provide experimental measurements of disk vibrations. These are then converted to off-track slider motions using the mode shapes of the disk and are correlated with the position error signal.

1.2 Motivation

The specific goals of this work are as follows:

1. To study the flow on both sides of a single spinning disk in a fixed hard drive casing, using large eddy simulation

2. To characterize the pressure loading on the disk and bring out the essential physical processes that take place in such flows

3. To develop an efficient and accurate solver to compute the free or forced vibrations of a spinning disk and to test the solver comprehensively

4. To use the solver to compute the response of the disk to realistic loadings, thus providing the disk drive community more realistic simulation results of the flow-induced disk vibrations

2 Theoretical Background

The equations of transverse motion of a spinning disk are well-known since Lamb and Southwell (1921). The governing equations may be extended to include the forcing due to the airflow excitation and the air bearing force due to the slider. These equations are given by,

$$\rho h \left(w_{,tt} + 2\Omega w_{,t\phi} + \Omega^2 w_{,\phi\phi}\right) + \frac{Eh^3}{12(1-\nu^2)}\nabla^4 w - \frac{h}{r}\left(\sigma_{rr} r w_{,r}\right)_{,r} - \frac{h\sigma_{\phi\phi}}{r^2} w_{,\phi\phi} = \Delta p + \frac{1}{r}\delta(r-\xi)\delta(\phi) f_z \tag{1}$$

Here, w is the transverse displacement of a point on the disk, ρ is the density of the disk material, h is the thickness of the disk, Ω is the speed of rotation of the disk, E and ν are the Young's modulus and Poisson's ratio of the disk material. The slider is modeled to exert a force f_z at a radius of ξ at $\phi = 0$ using the Dirac delta function $\delta(:)$. The unsteady distributed loading due to the airflow is given by $\Delta p = \Delta p(r, \phi, t)$. In polar coordinates, the biharmonic operator is given by,

$$\nabla^4 = \left(\frac{\partial^2}{\partial r^2} + \frac{1}{r}\frac{\partial}{\partial r} + \frac{1}{r^2}\frac{\partial^2}{\partial \phi^2}\right)^2 \tag{2}$$

Eqn. 1 assumes that the material of the disk is homogeneous, isotropic and linearly elastic (Hookean). The transverse displacements of the disk are assumed to be much smaller than the it's thickness ($w \ll h$) and the stress state of the disk is assumed to be plane stress (i.e. the disk remains relatively flat). Ω is also assumed to be constant. For a derivation of the full non-linear equations of motion the reader is referred to Chung et al. (2000). The self adjoint stiffness operator,

$$\mathbb{K}[w] = \frac{Eh^3}{12(1-\nu^2)}\nabla^4 w - \frac{h}{r}\left(\sigma_{rr} r w_{,r}\right)_{,r} - \frac{h\sigma_{\phi\phi}}{r^2} w_{,\phi\phi} \tag{3}$$

models the bending stiffness as well as the stiffness caused by the membrane stress tensor σ. The diagonal terms of the membrane stress tensor are σ_{rr} and $\sigma_{\phi\phi}$, while the off-diagonal term $\sigma_{r\phi}$ is assumed to be zero, by which we are assuming that the membrane stress in axisymmetric. The generalized plane stress solutions for the stress components σ_{rr} and $\sigma_{\phi\phi}$,

are,

$$\sigma_{rr} = c_1 + \frac{c_2}{r^2} - \frac{3+\nu}{8} r^2 \Omega^2 \tag{4}$$

$$\sigma_{\phi\phi} = c_1 - \frac{c_2}{r^2} - \frac{1+3\nu}{8} r^2 \Omega^2 \tag{5}$$

The constants c_1 and c_2 may be determined by the application of boundary conditions. The most commonly used model is to require that the displacement goes to zero at the inner clamp and the stresses go to zero at the free outer rim of the disk. (For some other models we refer the reader to the thesis of D'Angelo (1991)). Finally, the constants may be evaluated as,

$$c_1 = \Omega^2 \left(\frac{1+\nu}{8} \rho \frac{(\nu-1) r_o^4 - (3+\nu) r_i^4}{(\nu-1) r_o^2 - (1+\nu) r_i^2} \right) \tag{6}$$

$$c_2 = \Omega^2 \left(\frac{1-\nu}{8} \rho r_i^2 r_o^2 \frac{(1+\nu) r_o^2 - (3+\nu) r_i^2}{(\nu-1) r_o^2 - (1+\nu) r_i^2} \right) \tag{7}$$

where r_i and r_o denote the inner and outer radii of the disk.

There are four radial boundary conditions associated with Eqn. 1. At $r = r_i$, the transverse displacement and its rotation (slope) are zero,

$$w = 0; \qquad \frac{\partial w}{\partial r} = 0 \tag{8}$$

and at $r = r_o$ the radial bending moment and the shear force reaction are zero,

$$w_{,rr} + \nu \left(\frac{1}{r} w_{,r} + \frac{1}{r^2} w_{,\phi\phi} \right) = 0; \qquad (\nabla^2 w)_{,r} + (1-\nu) \frac{1}{r} \left[\left(\frac{1}{r} w_{,\phi} \right)_{,r} \right]_{,\phi} = 0 \tag{9}$$

Note that Eqn. 1 does not include any damping terms. Material damping of aluminum substrates used in hard disks is known to be significant (Kim et al., 2000). Hosaka and Crandall (1992) modeled this material damping as a term proportional to $\nabla^4 w_{,t}$. The other sources of damping are due to the clamping of the disk at its inner radius and the shear stress due to the drag of the flow on the disk surface. In our simulations each source of dissipation was not treated separately, but a global dissipation matrix was constructed from a linear combination of the mass and stiffness matrices (commonly referred to as proportional damping or Rayleigh damping). In supercritical vibrations of flexible disks, certain types of damping (e.g. acoustic damping and material damping) are known to cause the onset of flutter instabilities, in which case different sources of damping need to be modeled carefully (Kang and Raman, 2004). However, for our lower speed subcritical disks, a single proportional damping operator does suffice. The amount of dissipation for a range of frequencies was selected based on the aeroelastic parameters given in the experimental data of Kim et al. (2000). Typically, the first mode of the disk is damped at about 0.02% of critical damping.

3 Numerical Methods

Our calculations were broadly divided into two parts. In the first part, we calculated the flow of air in a simulated hard disk enclosure using a commercial CFD software and recorded the pressure data on the two sides of the disk as a function of time. In the next part of the calculation, we used this time-varying pressure data to compute the vibrations of the disk using a software program developed by us. The vibrations of the disk were not fed back into the CFD solver; thus the coupling was purely one directional, i.e. from the flow to the structure.

3.1 CFD methods

In our CFD work, we used large eddy simulation (LES) to simulate the airflow inside a realistic disk drive enclosure. A commercial code (CFD-ACE) using the Algebraic dynamic subgrid scale model (Germano et al., 1991) was used. A single 3.5 inch disk enclosed inside a fixed casing was used. The model used an e-block arm, suspensions, base plates and sliders.

Two cases were simulated:

1. Case 1: A single e-block arm, suspension, base plate and slider was used. The slider was in contact with the disk on the bottom surface only.

2. Case 2: Two e-block arms, suspensions, base plates and sliders were used. The disk was symmetrically actuated on both of it's surfaces.

Relevant details of the model geometry are given in Table 1, information regarding the CFD modeling is given in Table 2, boundary conditions are described in Table 3 and finally, the information regarding the grid is give in Table 4. A top view of the grid is also shown in Figure 1. With respect to Figure 1, we define a coordinate system, whose origin is at the center of rotation of the disks. Azimuthal angles are then defined counter-clockwise with respect to a horizontal line through the origin. Two angular positions are of special importance: the angle where the shroud separates from its circular shape to accommodate the actuator (located at about 220 degrees) and the angle where the shroud reattaches itself closely to the disk periphery (located at about 340 degrees). Figures 2 and 3 show the refinement of the grid in the vicinity of the actuator arm. Finally three dimensional outline views of the models are shown in Figures 4 (Case 1) and 5 (Case 2). Calculations were carried out on Linux based clusters, utilizing 64 CPUs at once. In spite of the massive computational horsepower, our simulations needed to run for several weeks.

3.2 Structural modeling

A finite-difference code based on central differencing was developed to simulate the vibrating disk. The linearity of Eqn. 1 and the periodicity of the azimuthal coordinate makes it a prime candidate for a hybrid-spectral method. Firstly, the primary variable w (transverse disk vibration) is Fourier transformed in the periodic direction (ϕ) resulting in a PDE of independent variables r and t.

$$w(r,\phi,t) = \sum_{m=-N/2+1}^{N/2} \hat{w}(r,t)e^{im\phi}; \qquad \frac{\partial}{\partial\phi} \rightarrow im \tag{10}$$

Transforming Eqn. 1, the following equation is obtained,

$$\begin{aligned}\rho h\left(\hat{w}_{,tt} + 2im\Omega\hat{w}_{,t} - m^2\Omega^2\hat{w}\right) + \frac{Eh^3}{12(1-\nu^2)}\hat{\nabla}^4\hat{w} - \frac{h}{r}\left(\sigma_{rr}r\hat{w}_{,r}\right)_{,r} \\ + \frac{m^2 h\sigma_{\phi\phi}}{r^2}\hat{w} = \Delta\hat{p} + \frac{1}{r}\delta(r-\xi)\delta(\phi)\hat{f}_z\end{aligned} \tag{11}$$

where,

$$\hat{\nabla}^4 = \left(\frac{\partial^2}{\partial r^2} + \frac{1}{r}\frac{\partial}{\partial r} - \frac{m^2}{r^2}\right)^2 \tag{12}$$

and $\Delta\hat{p}$ and $\hat{f}_z$ are the corresponding transformed pressure differential and slider force on the disk.

Central differencing is used for the radial direction. The Laplacian operator $\nabla^2 w$ is treated specially due to the polar coordinate system,

$$\begin{aligned}\nabla^2 w &= \left(\tfrac{\partial^2}{\partial r^2} + \tfrac{1}{r}\tfrac{\partial}{\partial r} - \tfrac{m^2}{r^2}\right)w = \left(\tfrac{1}{r}\tfrac{\partial}{\partial r}\left(r\tfrac{\partial w}{\partial r}\right) - \tfrac{m^2 w}{r^2}\right) \\ \Rightarrow \nabla^2 w_i &\approx \tfrac{1}{r_i}\tfrac{1}{\Delta r^2}\left(r_{i+\frac{1}{2}}(w_{i+1}-w_i) - r_{i-\frac{1}{2}}(w_i - w_{i-1})\right) - \tfrac{m^2 w_i}{r_i^2}\end{aligned} \tag{13}$$

This method is second order consistent and is easy to implement in an implicit time integration method. The other terms of Eqn. 1 are discretized using standard central differences.

Due to the spectral representation of one dimension of the primary variable, derivatives in ϕ are exact and are computed much faster than conventional finite differences. Moreover, due to the linearity of the equations, the different Fourier modes may be integrated independent of each other and forward and backward transforms need only be taken for initializing or post-processing the calculation.

3.2.1 Treatment of Boundary Conditions

The boundary conditions of Eqns. 8 and 9 are also discretized using central differencing, in the same manner as the governing equation. The governing equation (Eqn. 1) is discretized and solved for on all radial points in the domain. Since the central-difference stencil consists of 5 points (2 on each side of the central node), the numerical method requires the solution value at 2 additional points beyond the inner and outer boundaries of the disk. The addition of these "ghost points" is helpful in maintaining second order consistency of our method (Thomas, 1998). Finally, the solution values at the ghost points are expressed in terms of solutions in the actual domain by using the discretized boundary conditions.

3.2.2 Time integration

The well-known first order Newmark's algorithm is used for integrating Eqn. 1 in time. Since the method is implicit, a linear system needs to be inverted at every time step. However, since the Fourier modes are decoupled, a single global matrix may be constructed for each mode and inverted only at the start of the calculation. Thereafter, the calculation is progressed by the application of these stored inverted matrices. The principal advantage of using the Newmark's method over other conventional ODE integrators is the controllable numerical dissipation. Plots of the spectral radii of various Newmark's methods are widely available (Fung, 2003) and the Newmark two parameters (commonly referred to as β and γ) may be used to dissipate spurious high frequency oscillations in the solutions. Since the dissipation

introduced is only numerical, the frequencies of the modes do not shift, as they would when using a model for the material damping. Unless explicitly noted, all of our simulations used the standard values of $\beta = 0.5$ and $\gamma = 0.25$ which are non-dissipative.

4 Validation of the code

Validation of codes is an essential element of the code development process. Before we used our code to produce and report results, the code is put through a series of numerical tests and benchmarked against some well known data. First, some numerical tests of convergence are presented and then the code was validated against published results, such as for modal analysis and shock response. The comprehensive test results presented here should help readers in assessing the simulation numerical uncertainty of our work.

4.1 Tests of convergence

By a Taylor series expansion it is easy to see that our discretization scheme is second order consistent in the radial direction. In addition, the stability properties of the first order Newmark algorithm are also well known (unconditionally stable for $\beta \geq \frac{1}{2}$ and $\gamma \geq \frac{1}{4}\left(\frac{1}{2}+\beta\right)^2$) and carry over directly to our numerical scheme. For this reason, we directly prove the convergence of our code based on numerical experimentation.

Firstly, while keeping the time step constant, the radial mesh size is varied. The $\mathscr{L}_2$ norm of the absolute error (denoted by ϵ, based on the finest radial resolution (1.95×10^{-3})) is then computed and plotted as a function of the radial mesh size, as shown in Figure 8. The slope of the curve approximated by a linear curve fit is 1.87 which is close to the theoretical value of 2.0. This confirms that our central differencing scheme is convergent to second order in the radial direction.

Next, while keeping the radial mesh size constant, the time step is varied. While reduc-

ing the size of the time step (Δt) computations are carried out for correspondingly longer durations and solution values are recorded at 10 well defined points in time. The $\mathscr{L}_2$ norm of the absolute error (again, denoted by ϵ) is plotted as a function of (Δt) in Figure 9. While the data points do not fit a linear curve perfectly, the best curve fit to the data indicates an order of 0.7, which is close to the theoretical order of 1.0. Again, this proves that our implementation of the Newmark's algorithm is first order convergent.

4.2 Modal Analysis

As a test of validation for our code, we compare the modal frequencies obtained from our finite difference code with previously published theoretical and experimental data, and also results from the commercial code ANSYS.

In the thesis of D'Angelo (1991), a steel disk of outer diameter 356 mm, inner diameter 106.7 mm and thickness 0.775 mm was used to make measurements. Table 5 compares the natural frequencies of the modes of this stationary disk computed using our finite difference code with the theoretical and experimental prediction of D'Angelo (1991). The modes are described by a pair of integers (d, c) such that d is the number of nodal **d**iameters and c is the number of nodal **c**ircles. In our simulations, the impulse response of the disk was used to extract the modal frequencies. The theoretical calculations used a spectral Galerkin method while the the experimental setup used a inductance based Tektronic Modal Analyzer. Also included in Table 5 are the results obtained from the commercial code ANSYS. The results essentially show that our code can predict the natural frequencies of a stationary disk to reasonable accuracy. Generally, the discrepancies between our frequencies and the others increase with the mode number. The maximum difference between our results and the results across all columns is about 8%.

4.3 Shock Response

Our finite-difference simulator can easily simulate the application of a shock to the disk. Shocks are typically simulated as an acceleration field applied uniformly to the entire disk in the form of a half sine wave whose amplitude is described in Gs. Figure 10 shows the response of a stationary 1 inch disk to a 200 G amplitude shock applied for 0.5 milliseconds (wavelength of the sine wave is 1 ms). Both structural and numerical damping was used in the simulation: the Newmark parameter β was set to 0.55 and γ to 0.3.

The exact same shock condition simulated by a commercial code (ANSYS) is shown in Figure 11 reproduced directly from Bhargava and Bogy (2005). The Figures 10 and 11 show a very close agreement between our finite difference results and the finite element results of ANSYS. Figures 12 and 13 show the corresponding frequency spectra. The difference in the dominant frequency (3300 Hz) is approximately 6.06% while the difference in the next frequency peak (5500 Hz) is approximately 2.7%.

4.4 Variation of natural frequencies with RPM

As a final test, we demonstrate the ability of the code to predict the dynamics of disks under rotation. The modal analysis presented in Section 4.2 is for a stationary disk. It is well known that the (non-axisymmetric) disk modes split up into forward and backward traveling waves under rotation. Theoretically, in the absence of damping, the frequencies increase for forward traveling waves and decrease for backward traveling waves, with a slope equal to $d\Omega$, where d refers to the number of nodal diameters of the mode. The speed of rotation at which the backward wave becomes a stationary wave is the called the critical speed. Beyond the critical RPM, frequencies increase again, and the wave is called the reflected wave.

Figures 14-21 show the effect of rotation on several modes of the disk. Since the frequen-

cies of the modes are fairly close to each other, it is convenient to study the behavior of the modes separately. Generally, for a given number of nodal diameters, changing the number of nodal circles changes the frequency considerably, hence modes with the same number of nodal diameters, but different circles are visualized on the same Figure. The frequencies presented here are for a 3.5 inch disk that was used in our CFD simulations. The modes of the stationary disk computed using ANSYS are given in Table 6, and they compare well with the results presented in this Section. Table 6 also gives the theoretical frequencies of the modes at 10,000 RPM.

As expected, Figure 14 shows that the axisymmetric modes (0,0) and (0,1) do not form forward and backward waves. Figure 15 shows the formation of $(0,1)_{F,B}$ and $(1,1)_{F,B}$ and Figure 16 shows the formation of $(0,2)_{F,B}$ and $(1,2)_{F,B}$. Interestingly, mode $(0,2)_B$ goes critical at about 20,000 rpm which is shown more clearly in Figure 17. Similarly, $(0,3)_B$ in Figure 18 also goes critical at about 27,000 RPM which is shown in closely in Figure 17. Additionally, modes with 4 and 5 nodal diameters are shown in Figures 20 and 21. None of the remaining higher modes go critical before 30,000 RPM.

5 Discussion on CFD results

5.1 Characterization of Pressure loading

5.1.1 Mean and RMS values of the pressure loading

We begin by discussing the pressure loading on the disks. Figures 22 and 23 show the *resultant* mean pressure on the disks (averaged over 6 revolutions of the computational period) for Case 1 and Case 2 respectively. The resultant pressure is calculated as the sum of the pressure at the top and bottom surfaces of the disk – with positive pressures acting vertically out of the plane of the paper. Plots depicting the pressure may be non-

dimensionalized by $\frac{1}{2}\rho U^2_{\text{disk}}(r)$, but we refrain from doing this since it would be misleading to compare such pressure coefficients directly. The mean pressure is close to zero for Case 2 in almost all parts of the disk, because of the inherent (axial) symmetrical nature of the flow domain. The slight non-zero pressures at the edge of the disk (especially in the wake) are probably only numerical artifacts, occurring because the statistics may not have converged in that region.

The pressure distribution of Case 1 in Figure 22 shows some interesting features. Firstly, the resultant pressure is higher at the inner hub and lower at the outer hub. In Case 1, the lack of obstruction in the upper portion of the drive creates a strong radial pressure gradient. However, in the lower part of the model, the actuator blocks part of the flow, which equalizes the radial pressure gradient and increases the pressure upstream of the arm, especially nearer to the hub. The resulting asymmetry causes higher resultant pressure at the hub. Closer to the outer periphery, the shroud acts as a mechanism to equalize the pressure between the top and bottom parts of the drive, hence the resultant pressure load is smaller at the outer edges of the disk. The obstructing actuator creates a stagnating flow upstream, which leads to higher upstream pressures. This feature is also clearly manifested in Figure 22.

Figures 24 and 25 show the RMS of the resultant pressure variation on the disk surface. The RMS values are much higher at the edge of the disk (especially from the shroud separation to its reattachment), but the plots have a truncated color scale to accommodate most of the flow domain. Figures 24 and 25 show some similar features: 1) Large RMS pressure fluctuations at the periphery and smaller fluctuations at the inner hub. 2) A sharp increase in fluctuations at the shroud expansion. 3) Larger fluctuations in the wake formed behind the arm(s), and 4) Gradual reduction in the fluctuations downstream of the arm. Overall, the RMS for Case 2 is more than for Case 1 – which is a result of the turbulent flows on both sides of the disk. Finally, we also note that the presence of the arm causes a sharp break in axisymmetry, both in the mean and RMS. The loading process is thus non-uniformly dis-

tributed across several spatial scales (and time scales also, as we shall see) as characteristic of turbulent flows. Hence most analytical models cannot provide an accurate description of the loading.

5.1.2 Frequency contribution to the RMS

In addition to understanding the mean and RMS of the pressure loading, it is important to understand its spectral content. It is well known that turbulent flows in hard drives are composed of a broad range of forcing frequencies, distributed typically from 0-10 kHz (the distribution is strongly a function of the Reynolds number).

The RMS fluctuations of the pressure broken up into contributions from various frequency bands are shown in Figures 26- 31 for Case 1 and Figures 32- 37 for Case 2. In each figure, the RMS pressure fluctuations are plotted as a function of the radius, from OD to ID. The RMS contribution across different frequency bands may be easily computed using the Parseval's theorem.

Figure 26 shows the fluctuations in the near wake region (326 degrees from the origin). In this position, we notice the high fluctuations in the outer portion of the disk which is being impacted by the eddies shed from the arm. These fluctuations are comparable to the mean value of the pressure itself. The majority contribution to the fluctuations is from the low frequency components, 0-1 and 1-2 kHz. Towards the ID, fluctuations are much smaller, and are almost solely composed of the low frequency 0-1 kHz forcing. The peak in RMS is not located at the edge of the disk but at one position before the OD. As the flow progresses azimuthally, the fluctuations on the disk damp out quickly. Figure 27 shows the fluctuations at 0 degrees. The RMS values are about half of what they were 34 degrees upstream. This rapid reduction of fluctuations appears across all frequency bands. As the flow progresses through the rest of the drive, the overall fluctuations reduce through the effects of viscous and SGS dissipation. The effects of the wake appear to move from the OD to the MD in

Figures 28 and 29 and the fluctuations are almost completely dissipated by 180 degrees in Figure 30. A common observation in Figures 28 through 30 is the relatively higher RMS at the edge of the disk. The higher RMS values are due to the turbulent flow in the shroud gap and the resulting forcing has RMS contributions from higher frequencies, up to 10 kHz. Finally, an interesting consequence of the shroud expansion is shown in Figure 31 at 236 degrees from the origin. The figure shows very high fluctuations at the outer edge of the disk with significant contributions from 0-1, 1-2 and 2-6 kHz frequencies. Apparently, the shroud expansion causes massive flow separation and generation of turbulence, with intensities that are comparable with those in the wake of the arm.

For completeness, Figures 32- 37 show the RMS pressure plots for Case 2, for the same angular positions as in Case 1. The Figures show that Case 2 has slightly higher fluctuations compared to Case 1, due to the turbulence generated on both sides of the disk. The Figures for Case 2 demonstrate much of the same qualities as discussed above for Case 1: high RMS fluctuations in the wake, high frequency contributions to fluctuations due to the flow in the shroud gap and very high RMS due to the shroud expansion.

5.2 Axial flow in the shroud

The RMS of the axial flow in the shroud gap (i.e. the component of the flow perpendicular to the plane of the disks) is shown in Figure 38 . for the complete azimuthal span (0-360) for three different axial positions: $z = 3.3$ corresponds to the top surface of the disk, $z = 2.8$ corresponds to the mid-plane of the disk and $z = 2.3$ corresponds to the bottom surface of the disk. The axial velocity is non-dimensionalized, not by the mean axial velocity but by the disk edge velocity (Ωr_o), since the former is close to zero. The RMS fluctuations of pressure at the same location as Figure 38 are shown in Figure 39. The strong correlation between the axial velocity fluctuations and the pressure fluctuations is clearly evident by comparing Figures 38 and 39. Finally, a three dimensional view which shows the locations

of the different peaks in the RMS axial velocity fluctuations is shown in Figure 40.

We notice that the fluctuations are fairly constant in the shrouded portion of the drive, with a very gradual decrease in the amplitude downstream of the wake. The RMS of the fluctuations is a measure of the amplitude of the waves that the shroud gap can support. In both cases, the RMS amplitude is small; close to 2% of the disk edge velocity. The presence or absence of an actuator simply does not matter, as there is very little difference between the Cases 1 and 2. In agreement with our previous discussion, the shroud expansion causes very high fluctuations in the axial velocity (seen as the first large spike at about 220 degrees in Figure 38). The axial velocity fluctuates rapidly as the flow approaches and flows over the arm. The wake is characterized by a single peak immediately downstream of the arm, and several other peaks as the flow gets entrained back into the shrouded portion of the gap.

Figure 40 shows the location of these peaks three dimensionally. Also in Figure 40, at a particular axial location, three curves are drawn spanning the width of the shroud gap. For both cases, one notices that the outermost curve does not show a peak of the same magnitude of the inner two curves at the shroud expansion. This indicates that the high fluctuations associated with the separation are present close to the disk edge only and apparently die down shortly beyond the disk edge.

5.3 Velocity profiles

Much about the flow can be understood by studying the average velocity profiles between the disk and the stationary casing walls. Figures 41 and 42 show the time averaged non-dimensional velocity profile $\left(\frac{\overline{u_\phi}(r)}{\Omega r}\right)$ as a function of the axial position between the disks. The central solid band in the Figure represents the disk. The profiles are shown, horizontally for different azimuthal positions (0-320 degrees) and vertically, for three radial positions, ID, MD & OD. Each horizontal box spans the non-dimensional magnitude from 0 to 1, while each vertical box spans the entire axial length of the domain, as shown: from the bottom

cover to the top cover. Azimuthal positions are measured from the horizontal with respect to the disk centers, with the actuator being located at about 280 degrees at MD.

In Figure 41, which is for Case 1, one immediately observes the asymmetry of the velocity profiles. As expected, velocity profiles below the disk are smaller in magnitude than those above the disk, which is due to the loss in momentum by flowing over the arm. At about 240-280 degrees we observe that the flow stagnates in the space below the disk – which is most likely due to the blocking effects of the actuator. Interestingly, the flow also stagnates in the space above the disk at the ID position (i.e. close to the hub). Since, there is no arm present in this portion of the drive, the only reason for the formation of this re-circulating flow would be the expanding section of the geometry. To clarify: once the flow has passed through the shrouded portion of the drive, it encounters an expanding section (to accommodate for the actuator). This expansion causes the flow to reverse direction close to the hub, where the linear velocity of the disk is the smallest. On the bottom side of the disk, the actuator blocks some of the expanded section, accelerating the flow slightly – which results in a higher velocity of the flow at 280-320 degrees.

Velocity profiles for Case 2 in Figure 42 are more symmetric than Case 1. Since the geometry, grid and boundary conditions are perfectly mirrored across the midplane, any lack of symmetry can only be attributed to insufficient data in the averaging process. In general, the velocity profiles look very similar to a turbulent Couette flow. There is a sharp fall off from the disk velocity in the boundary layer, a large core region of nearly constant velocity flow, followed by a sharp fall off to the stationary wall. It is also a general observation that the velocity profile is not completely flat in the central core region. Velocities are slightly higher in the region away from the disk. This can be mainly attributed to the axial location of the actuator. Referring to Figures 6 and 7, the actuator is located closer to the disk than the fixed covers, hence the flow is decelerated in this region and accelerated closer to the covers. Figure 42 also shows the following features of the flow: 1) The flow stagnates near

the hub, upstream of the actuator arm. 2) The velocity profile is small in the wake of the actuator and becomes fuller as it progresses azimuthally. 3) From about 80 degrees to about 200 degrees the velocity profiles are very similar across ID-MD-OD positions. 4) Almost all velocity profiles have an inflection point near the disk

5.4 Global Quantities

The non-dimensional kinetic energy (k^*) and windage (W^*) are plotted in Figures 43 and 44 as a function of the number of disk rotations. Let U_o be the disk edge velocity, $\mathbb{V}$ be the volume of the computational domain, $\mathbb{A}$ be the area of the computational box, ν be the dynamic viscosity, $\overline{S_{ij}} = \frac{1}{2}\left(\frac{\partial \overline{U_i}}{\partial x_j} + \frac{\partial \overline{U_j}}{\partial x_i}\right)$ be the filtered rate-of-strain tensor and τ_{ij}^R be the sub-grid scale (residual) stress tensor. The following quantities may then be defined as:

$$\begin{aligned} U_o &= \Omega r_o \\ \mathbb{V} &= \int_{\mathscr{V}} dV \\ \mathbb{A} &= \int_{\partial\mathscr{V}} dA \end{aligned}$$

$$k^* = \frac{\frac{1}{2}\int_{\mathscr{V}} \mathbf{u}\cdot\mathbf{u} dV}{\frac{1}{2}U_o^2 \mathbb{V}} \tag{14}$$

$$W^* = \frac{\int_{\partial\mathscr{V}} \left(2\nu\overline{u_j}\overline{S_{ij}} - \overline{u_j}\tau_{ij}^R\right) dA}{\left[\frac{1}{2}U_o^2\right][U_o]\,\mathbb{A}} \tag{15}$$

From Figures 43 and 44 we notice that the kinetic energy in Case 2 is approximately 10% less than Case 1, which may be accounted for by the turbulent loss caused by the addition of an extra arm. However, the windage loss (i.e. the power required to drive the disks, or the rate of energy input to our computational domain) is about 2.5% smaller for Case 2 than for Case 1. This implies that with a slightly smaller rate of energy input, the Case 2 simulation

saturates at a lower energy level, indicating the increased presence of dissipative processes such as vortex shedding and separation.

In reporting the kinetic energy and windage, the role of the initial conditions of the domain has been minimized by starting off both the simulations from a steady $k-\epsilon$ solution. Moreover, the figures also show that the quantities achieve steady state in about 4 revolutions of the disk which gives confidence that the simulations have achieved statistical steadiness on a global level. For this reason, all quantities reported previously are only for the duration spanning 4 to 10 revolutions of the simulations.

The coefficients of drag on the actuator arm are plotted as a function of time (with the first 4 revolutions removed) in Figure 45 and the corresponding frequency spectra are plotted in Figure 46. The drag and lift coefficients are decomposed into the off-track direction ($C_{D,off}$), the on-track direction ($C_{D,on}$) and the axial (out-of-plane) direction ($C_{D,z}$) using the projected areas of the actuator in those directions and the disk edge speed $U_o = \Omega r_o$. Figures 47, 48 and 49 summarize the statistics of the data in the Figure 45. Interestingly, the figures show that the mean off track drag coefficient,$\overline{C_{D,off}}$, is higher in Case 2 than in Case 1, but the trend is opposite for the on-track direction, $\overline{C_{D,on}}$. The additional e-block arm, suspension, base plate and slider in Case 2 increases the off-track projected area by only 25%, while the on-track projected area is the same. This indicates that the presence of the symmetric arms in Case 2 modifies the pressure field in the drive, such that the pressure gradient acting across the arm (in the off-track direction) is increased while the gradient in the direction of the arm (the on-track direction) is decreased.

6 Structural vibrations

Next the vibrations of the disk are calculated using the code previously discussed. The vibrations are initialized from rest and the pressure loading of the airflow and the slider are

used as forcing functions on the right hand side. An (r, m) grid of 32×64 was used and the resultant pressure recorded at each of the 2048 nodes was used in the calculation. The slider was modeled as a point load (delta function) superimposed on the airflow pressure distribution.

The vibrations of the disk are plotted as a function of time in Figure 50 for both Cases 1 and 2. In plotting the displacements of the disk, since the vibrations under the slider are most important, various points were chosen from ID to OD passing through the location of the slider. The 6 sub-figures shown in Figure 50 are plotted for points located at 12.5%, 31.25%, 50% (MD), 62.5 %, 81.25% and 100% (OD) of the radial span.

We notice that the vibrations have a positive bias (mean) for Case 1 which is expected given the positive mean pressure. The mean vibrations for Case 2 are close to zero. The vibrations of Case 2 clearly display a fundamental frequency (which from Table 6 is attributed to mode $(0, 1)_B$). Case 1 does not clearly display this frequency and is apparently composed of higher frequency components. The other interesting observation is that the vibration results appear to be a linear function of the radius; i.e. the sub-figures of Figure 50 appear to be geometrically very similar except for the different scale used to plot them. This leads to the conclusion that most of the vibration energy is in the modes with zero nodal circles (c=0). Given that the pressure fluctuations of the flow are mainly in the low frequencies (0-2kHz) (recall, Figures 26- 37), such a result is expected, since the first mode with one nodal circle (c=1) is above 5 kHz and there are 6 modes of lower frequency than 5kHz (with their corresponding forward and backward traveling frequencies. See Table 6).

A summary of the vibration results is presented in Figure 51. It shows that the disk has a mean deflection for Case 1, due to the mean pressure bias. The RMS vibrations about that mean are smaller than those for Case 2, but the resulting motions are larger for Case 1. The mean vibrations for Case 2 should theoretically be zero, but the small non-zero mean is a result of unconverged statistics. The RMS vibrations for Case 2 are

large, approximately 680 nm. The results presented in Figure 51 are in good agreement with experimental measurements of the disk vibrations, given in Imai (2001), Chang et al. (2002) and Guo and Chen (2001).

Due to the large number of modes in the 0-5Hz range, the frequency spectra for the vibrations cannot be easily analyzed visually. It is more useful to understand the contributions to the RMS from different frequency bands, as done earlier for the pressure fluctuations. As seen in Figure 52, for Case 2, approximately 95% of vibration energy is in the 0-1 kHz range, which contains the top three modes. A small amount of energy is contained in the 1-5 kHz range, while there is virtually no contribution thereafter. This is the reason why the dominant frequency of Case 2 in Figure 50 corresponds to the $(0, 1)$ mode. For Case 1, approximately 20% of the energy is shifted from the 0-1 kHz range to the 1-5 kHz range. Given the mean deflection of the disk about its equilibrium, energy is transferred from the $(0, 1)$ mode to higher modes (mode # 4-6) and this results in a smaller RMS amplitude of vibration.

7 Conclusions and Future Work

To summarize:

1. We have presented a methodology for computing the vibrations of the rotating disk in a hard disk drive, dealing with much more realistic air flow models than previous attempts. Given the complicated nature of the flow, calculations need to be repeated for even small changes to the drive configuration, (e.g. movement of the actuator from ID to OD), which makes a comprehensive investigation of all cases very expensive; almost impossible. However, we have provided two useful aids in the solution to such problems. 1) We have characterized the pressure loading in great detail for the two most commonly occurring cases (sliders flying on one or two sides of the disk) and

2) We have described the numerical methods to accurately compute the flow and the structural solutions. Finally, we expect that the data presented will serve as a useful tool for benchmarking future calculations or experiments

2. In terms of the flow field, we found that the mean pressure loading for Case 1 is asymmetric, arising due to the asymmetry of the geometrical configuration. The RMS vibrations of Case 2 are higher than those for Case 1 and their spectral distributions are almost identical. The spectra show most of the energy is in the 0-1 kHz range and the RMS increases with increasing radius. The wake and the shroud expansion show the highest fluctuations. While the formation of the wake behind the arm is inevitable, drive designers should avoid expanding diffuser-like cross-sections which act as a source of separation and generation of turbulence. We also found that the fluctuations in the shroud gap corellate very well with the pressure fluctuations – hence, it may be useful to measure the axial flow in the gap (say by PIV) when measurement of pressure is difficult. Finally, we also note that the velocity profiles between the disk and the casing resemble turbulent Couette flow very well, and may be used to model flows in other cases.

3. In terms of the disk vibrations, we note that 1 mm thick 3.5 inch Aluminum disks may be susceptible to critical behavior at about 20,000 RPM. Our results do not take into account changes in the flow field at those speeds and the resulting damping. Nonetheless, drives that operate in the 20,000-30,000 RPM range may be subject to these resonances. At 10,000 RPM our results show that for Case 1 the disk undergoes a mean asymmetric deflection and vibrates at a smaller magnitude in the higher modes. For Case 2, there is no mean deflection, and the disk primarily vibrates in the lowest fundamental mode.

4. A direct continuation of this work would be to compute the resulting off-track and

on-track motions of at the slider-head, both due to the air drag and the disk motion. While this is currently unfeasible in our simulations, given the separation of scales, this could be the subject of another investigation that accounts for all the non-linear dynamics of the slider motion.

Acknowledgment

This study was supported by the Computer Mechanics Laboratory (CML) at the University of California, Berkeley.

The authors wish to acknowledge the contribution from Intel Corporation, Hewlett-Packard Corporation, IBM Corporation, and the National Science Foundation grant EIA-0303575 in making hardware and software available for the CITRIS Cluster which was used in producing these research results.

References

P. Bhargava and David B. Bogy. Numerical simulation of operational-shock in small form factor drives. *CML Report*, 05-005, 2005.

Y-B. Chang, D-K Park, N-C Park, and Y-P Park. Prediction of track misregistration due to disk flutter in hard disk drive. *IEEE Transactions on Magnetics*, (2):1441–1446, 2002.

J. Chung, J.-E. Oh, and H. H. Yoo. Non-Linear Vibration of a Flexible Spinning Disc with Angular Acceleration. *Journal of Sound Vibration*, 231:375–391, March 2000.

C. D'Angelo. *Vibration and Aeroelastic stability of a Disk Rotating in a Fluid*. PhD thesis, University of California, Berkeley, 1991.

R. Fukaya, S. Obi, S. Masuda, and M. Tokuyama. Flow instability and elastic vibration of shrouded corotating disk systems. *Experiments in Fluids*, 33:369–373, July 2002.

T. C. Fung. Numerical dissipation in time-step integration algorithms for structural dynamic analysis. *Progress in Structural Engineering and Materials*, (3):167–180, 2003.

M. Germano, U. Piomelli, P. Moin, and W. H. Cabot. A dynamic sub-grid scale eddy viscosity model. *Physics of Fluids*, A(3):1760–1765, 1991.

L Guo and Y-J. D. Chen. Disk flutter and its impact on hdd servo performance. *IEEE Transactions on Magnetics*, 37(2):866–870, 2001.

H. Hosaka and S. Crandall. Self-excited vibrations of a flexible disk rotating on an air film above a flat surface. *Acta Mech.*, 3:115–127, 1992.

S. Imai. Fluid dynamics mechanism of disk flutter by measuring the pressure between disks. *IEEE transactions on magnetics*, 37(2):837–841, 2001.

N. Kang and A. Raman. Aeroelastic flutter mechanisms of a flexible disk rotating in an enclosed compressible fluid. *Journal of Applied Mechanics (Transactions of the ASME)*, 71(1):120–130, 2004.

B. C. Kim, A. Raman, and C. D. Mote. Prediction of Aeroelastic Flutter in a Hard Disk Drive. *Journal of Sound Vibration*, 238:309–325, November 2000.

H. Lamb and R. V. Southwell. The Vibrations of a Spinning Disk. *Royal Society of London Proceedings Series A*, 99:272–280, July 1921.

M. Tatewaki, N. Tsuda, and T. Maruyama. A numerical simulation of unsteady airflow in hdds. *FUJITSU Sci. Tech. J.*, 37(2):227–235, 2001.

J. W. Thomas. *Numerical Partial Differential Equations: Finite Difference Methods*. Springer, 1998. ISBN 0387979999.

J. P. Van doormaal and G. D. Raithby. Enhancements of the simple method incompressible fluid flows. *Numerical Heat Transfer*, 7:147–163, 1984.

Z. X. Yuan, A. C. J. Luo, and X. Yan. Airflow pressure and shear forces on a rotating, deformed disk in an open shroud. *Communications in Nonlinear Science and Numerical Simulation*, 9(5):481–497, 2004.

8 Tables

Table 1: Geometry data

	Case 1	Case2
Number of disks	1	←
Number of e-block arms	1	2
Number of base plates	1	2
Number of suspensions	1	2
Number of sliders	1	2
Disk thickness (mm)	1	←
Disk diameter (mm)	76.2	←
Width of shroud gap (mm)	1	←
Length of actuator (mm)	45	←
Length of e-block arm (mm)	32.5	←
Length of base plate (mm)	6.5	←
Length of suspension (mm)	11.1	←
Thickness of e-block arm (mm)	0.8	←
Thickness of base plate (mm)	0.3	←
Thickness of suspension (mm)	0.1	←
Dimensions of slider (mm)	$1 \times 0.8 \times 0.3$	←
Number of weight saving holes in e-block arm	2	←

]

Table 2: CFD modeling information

Governing equations	Filtered Navier Stokes equations
Solution algorithm	SIMPLEC (Van doormaal and Raithby, 1984)
Large eddy simulation model	Algebraic dynamic (Germano et al., 1991)
Type of LES filter	Top-hat (variable width)
Temporal differencing scheme	Crank Nicholson (second order)
Spatial differencing scheme (convective term)	Central differencing
Time step (seconds)	1.0×10^{-5}
Number of time steps	4800
Corresponding number of disk rotations	8
Initial conditions	Steady k-ϵ solution

Table 3: Boundary conditions

Disks	Rigid rotating walls, no slip
Casing	Rigid wall, no slip
Hub/base of e-block arm	Fixed (similar to a cantilever)
Slider-disk interface	Slider slips on disk No cells between slider and disk
All structural interfaces (e.g. suspension+slider, e-block arm+base plate)	Rigidly joined (i.e. no dimple)
All fluid-structure surfaces	walls, no slip

Table 4: Grid information

	Case 1	Case 2
Type of mesh	Structured grid mixed with quad-dominant unstructured cells	←
Number of cells.	4,515,444	4,444,274
Avg. cell vol. (mm^3)	5.7338×10^{-3}	5.7994×10^{-3}
Avg. grid res. (mm)	0.1789	0.1796

Table 5: Comparison of natural frequencies of a stationary disk

Mode	Current Work (Hz)	Experiments (Hz)	% Diff	Theory (Hz)	% Diff	ANSYS (Hz)	% Diff
(0,1)	36	37.19	3.20	39.08	7.88	38.06	5.41
(0,0)	40	38.40	-4.17	39.73	-0.68	38.68	-3.42
(0,2)	46	47.10	2.34	47.46	3.08	46.20	0.44
(0,3)	77	79.78	3.48	79.18	2.75	77.10	0.13
(0,4)	124	133.08	6.82	131.64	5.80	128.30	3.35
(0,5)	189	202.18	6.52	200.16	5.58	195.27	3.21
(1,0)	236	250.18	5.67	254.18	7.15	247.31	4.57
(1,1)	246	262.38	6.24	266.23	7.60	259.00	5.02
(0,6)	269	285.71	5.85	282.68	4.84	276.19	2.60
(1,2)	280	304.79	8.13	303.88	7.86	295.50	5.25
(1,3)	348	374.92	7.18	370.12	5.98	359.53	3.21

Note: Experimental and theoretical data is from D'Angelo (1991)

Table 6: Natural Frequencies and modes of the disk, obtained from ANSYS

Mode No.	**Frequency (Hz)**	**Mode (d,c)**	**Forward Mode @ 10K RPM**	**Backward Mode @ 10K RPM**
1	**781.56**	(1,0)	948.23	614.89
2	**802.71**	(0,0)	–	–
3	**946.65**	(2,0)	1279.98	613.32
4	**1610.9**	(3,0)	2110.90	1110.90
5	**2704.4**	(4,0)	3371.07	2037.73
6	**4126**	(5,0)	4959.33	3292.67
7	**5104.3**	(0,1)	–	–
8	**5355.1**	(1,1)	5521.77	5188.43
9	**5837.6**	(6,0)	6837.60	4837.60
10	**6147.3**	(2,1)	6480.63	5813.97
11	**7552.3**	(3,1)	8052.30	7052.30
12	**7826.9**	(7,0)	8993.57	6660.23
13	**9588.1**	(4,1)	10254.77	8921.43
14	**10090**	(8,0)	11423.33	8756.67
15	**12194**	(5,1)	13027.33	11360.67
16	**12624**	(9,0)	14124.00	11124.00
17	**14773**	(0,2)	–	–
18	**15071**	(1,2)	15237.67	14904.33
19	**15271**	(6,1)	16271.00	14271.00
20	**15430**	(10,0)	17096.67	13763.33
21	**15991**	(2,2)	16324.33	15657.67
22	**17599**	(3,2)	18099.00	17099.00
23	**18507**	(11,0)	20340.33	16673.67
24	**18736**	(7,1)	19902.67	17569.33
25	**19951**	(4,2)	20617.67	19284.33
26	**21855**	(12,0)	23855.00	19855.00
27	**22541**	(8,1)	23874.33	21207.67
28	**23065**	(5,2)	23898.33	22231.67
29	**25475**	(13,0)	27641.67	23308.33
30	**26659**	(9,1)	28159.00	25159.00

9 Figures

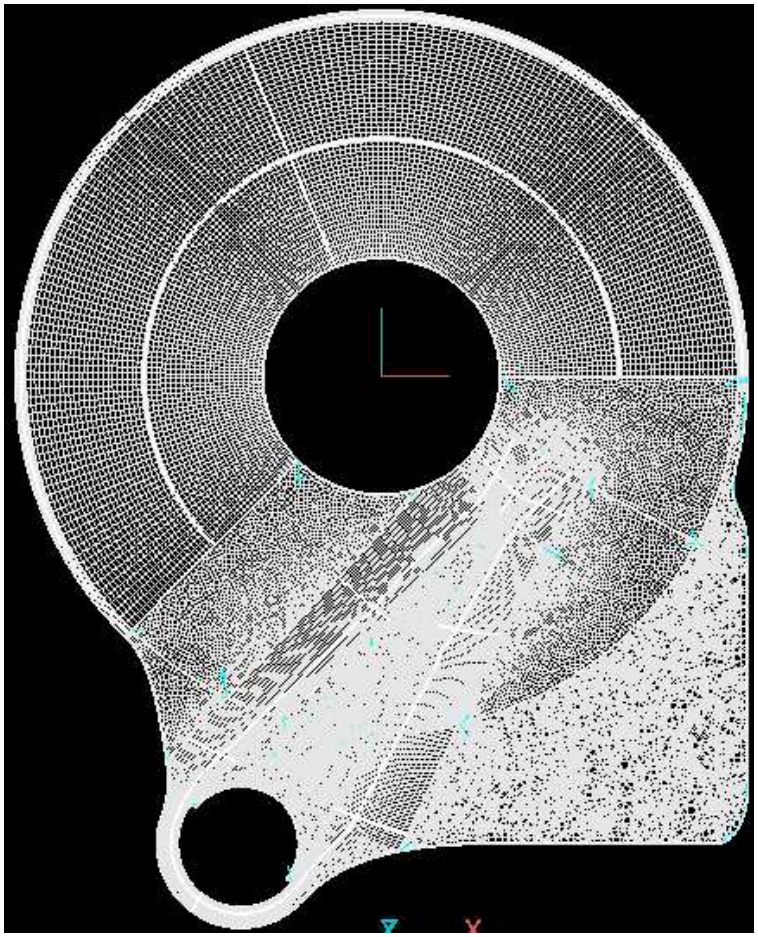

Figure 1: Top view of the computational grid

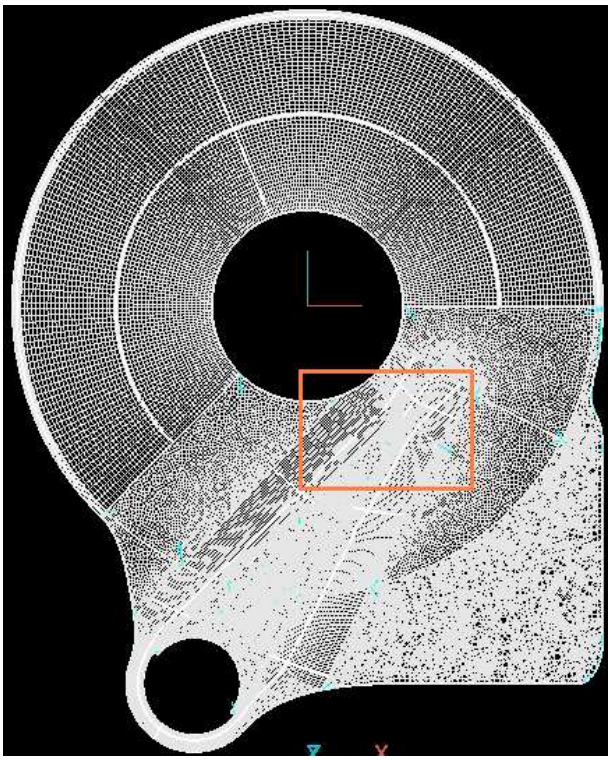

Figure 2: Location of closeup in Figure 3

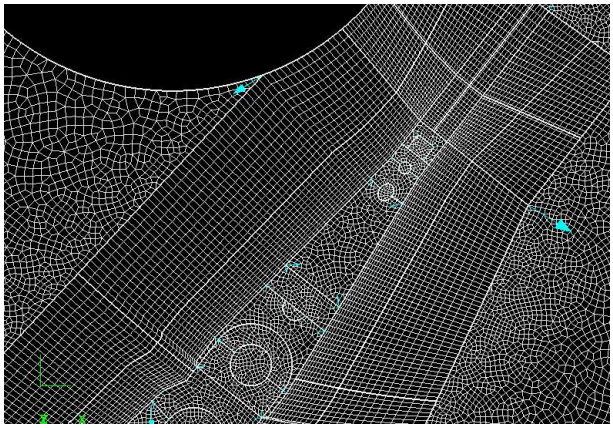

Figure 3: A closeup view of the refined grid upstream and downstream of the actuator

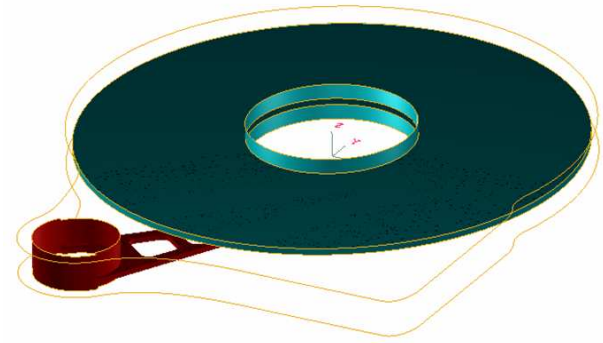

Figure 4: Three-dimensional simplified view of the simulated Case 1. Shown are the disk and the single arm actuating the lower surface

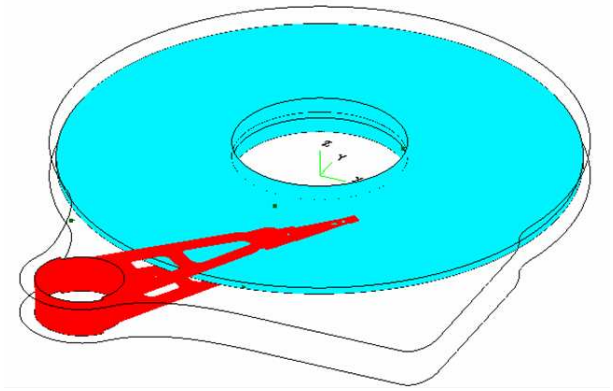

Figure 5: Three-dimensional simplified view of the simulated Case 2. Shown are the disk and the arms on both the disk surfaces

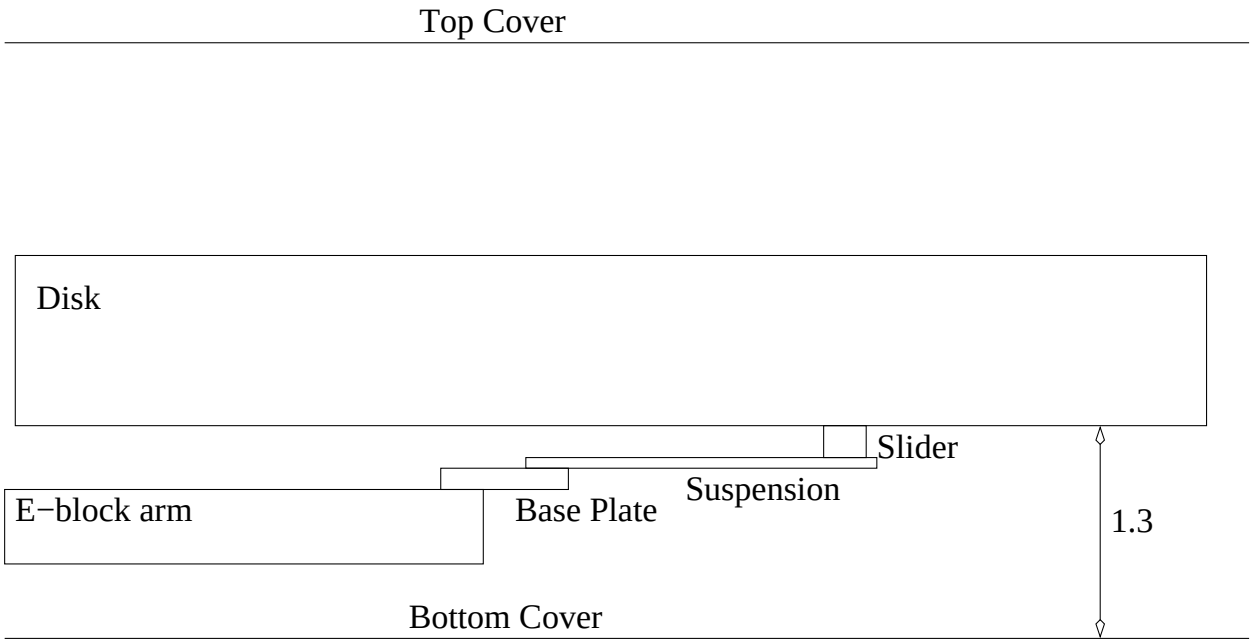

Figure 6: Schematic diagram showing cross section of simulation domain for Case 1

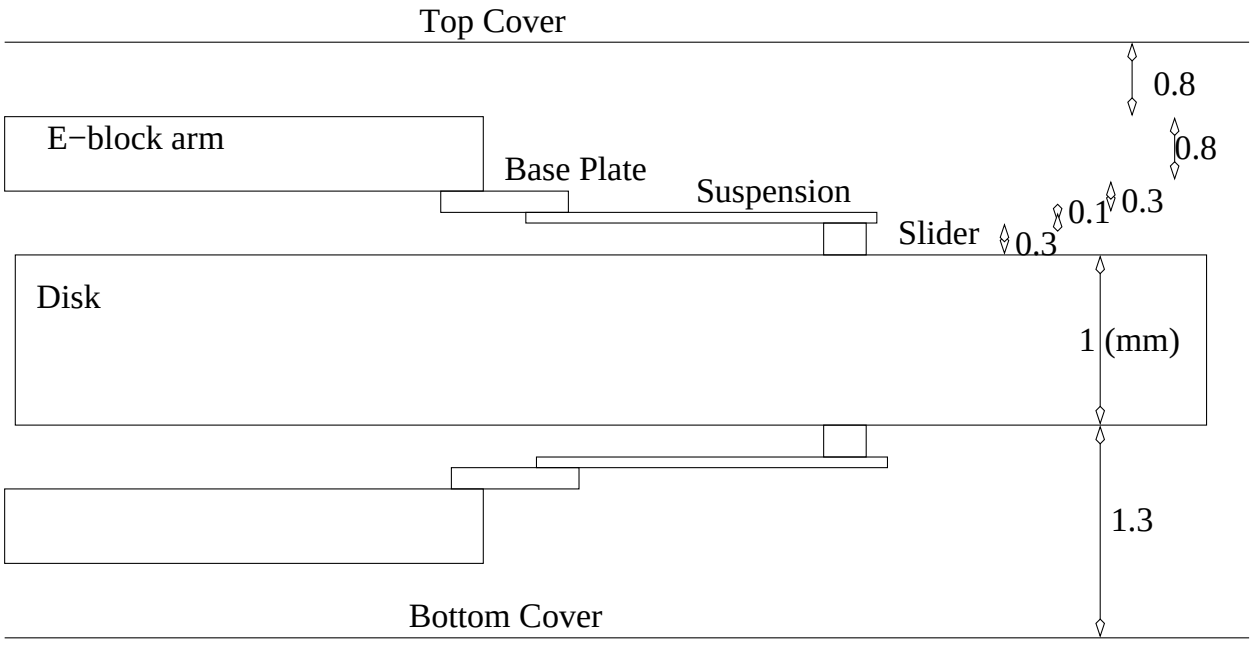

Figure 7: Schematic diagram showing cross section of simulation domain for Case 2

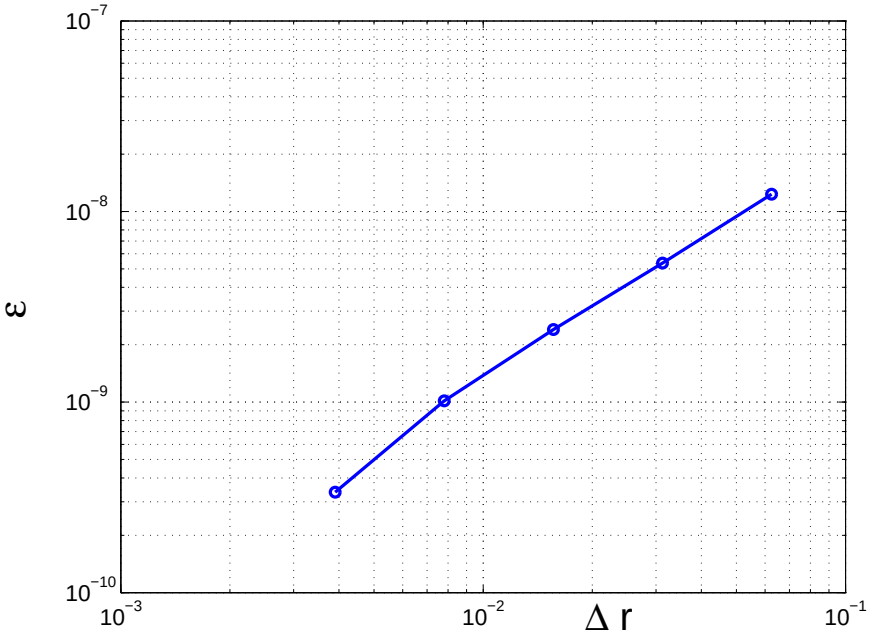

Figure 8: Radial convergence: $\mathscr{L}_2$ norm of the error (ϵ) as a function of the radial mesh size (Δr)

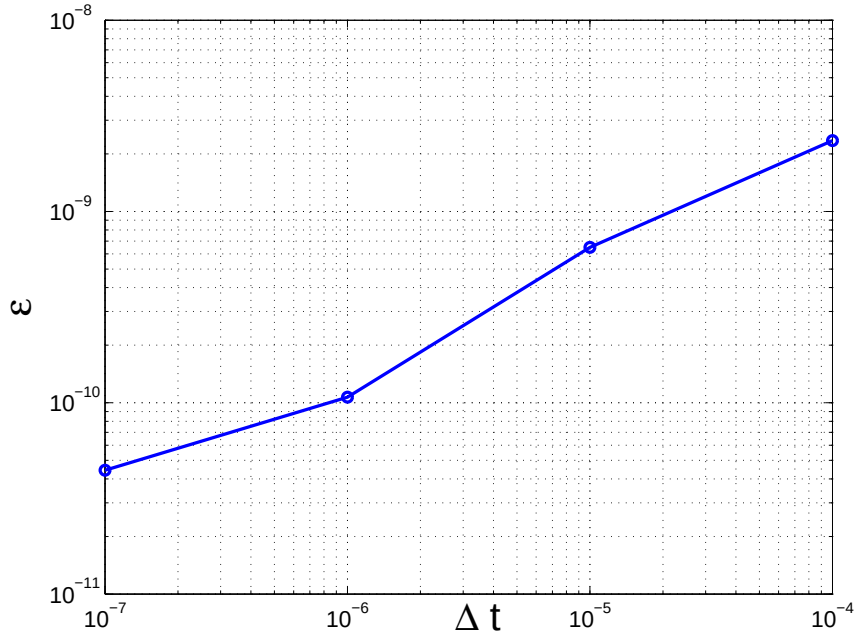

Figure 9: Radial convergence: $\mathscr{L}_2$ norm of the error (ϵ) as a function of the time step (Δt)

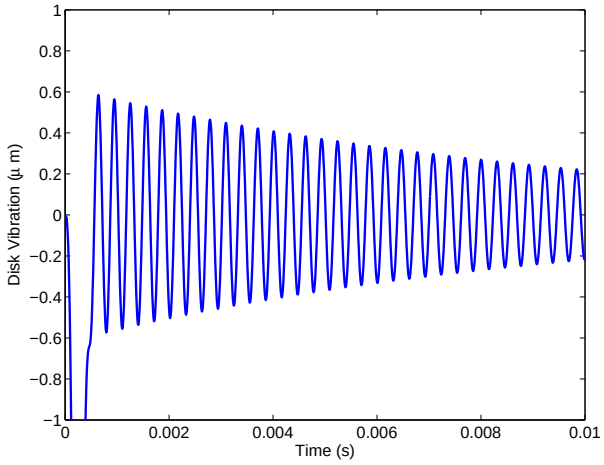

Figure 10: Response of a disk to 200 G shock of 0.5 milliseconds. computed using current code

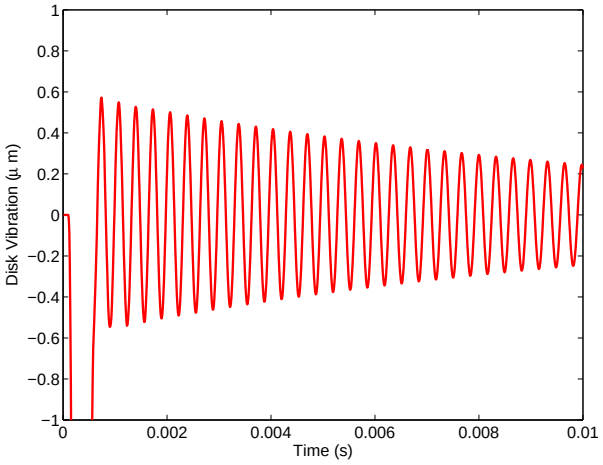

Figure 11: Response of a disk to 200 G shock of 0.5 milliseconds. computed using ANSYS (Bhargava and Bogy, 2005)

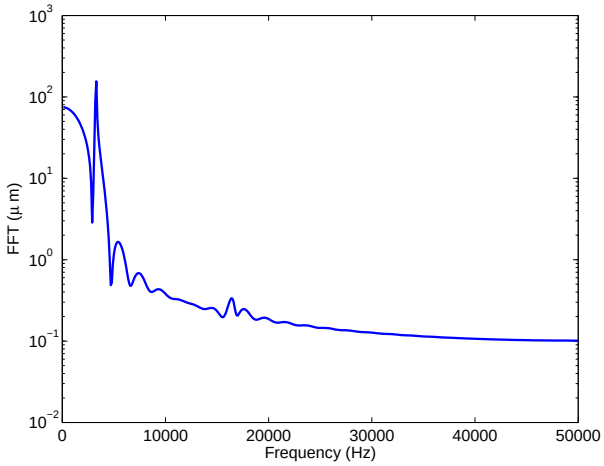

Figure 12: FFT of disk response to 200 G shock of 0.5 milliseconds. computed using current code

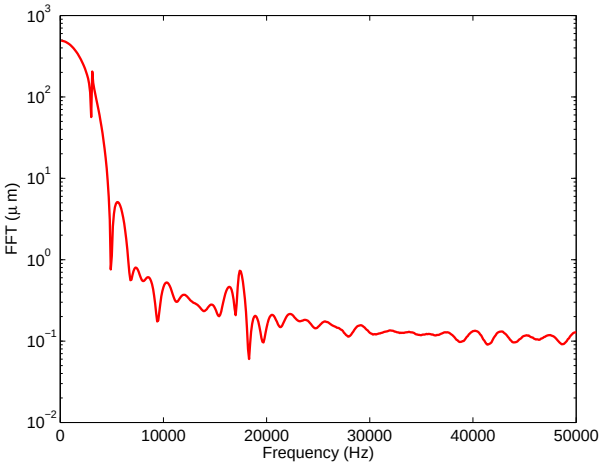

Figure 13: FFT of disk response to 200 G shock of 0.5 milliseconds. computed using ANSYS (Bhargava and Bogy, 2005)

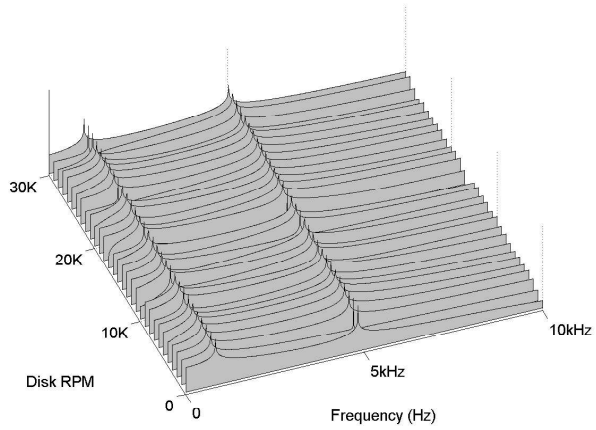

Figure 14: Waterfall plot showing the natural frequencies as a function of RPM. Modes (0,0) and (1,0)

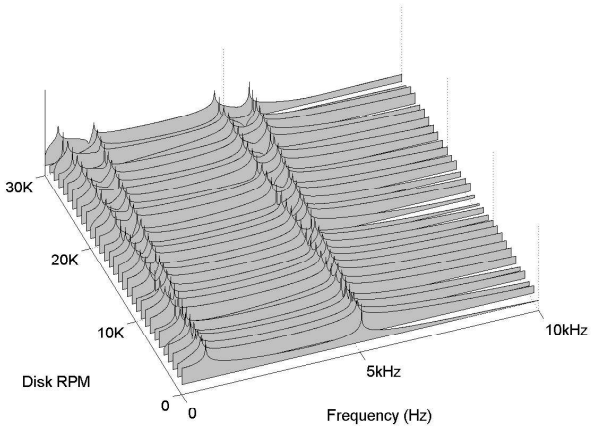

Figure 15: Waterfall plot showing the natural frequencies as a function of RPM. Modes (0,1) and (1,1)

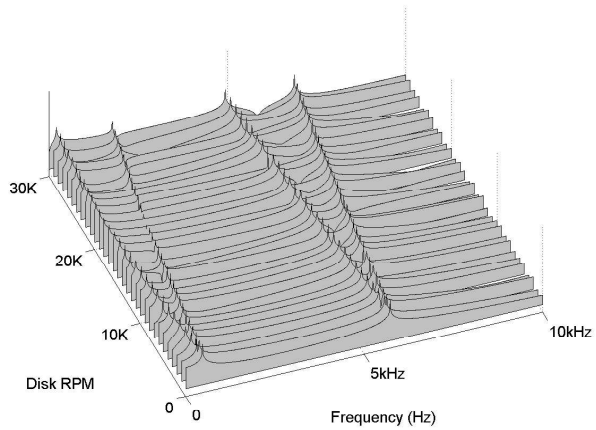

Figure 16: Waterfall plot showing the natural frequencies as a function of RPM. Modes (0,2) and (1,2)

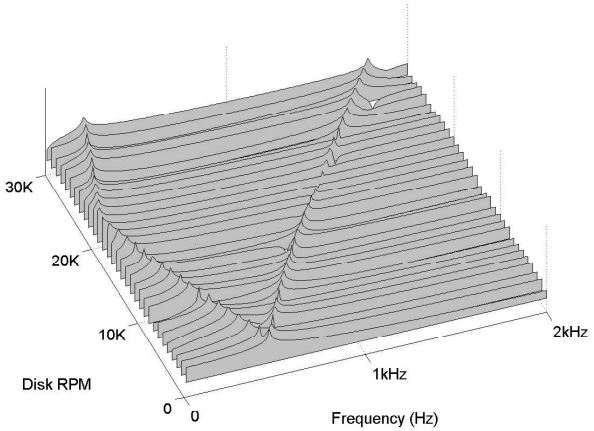

Figure 17: Closeup showing the critical behavior of mode $(0,2)_R$ at 20,000 RPM

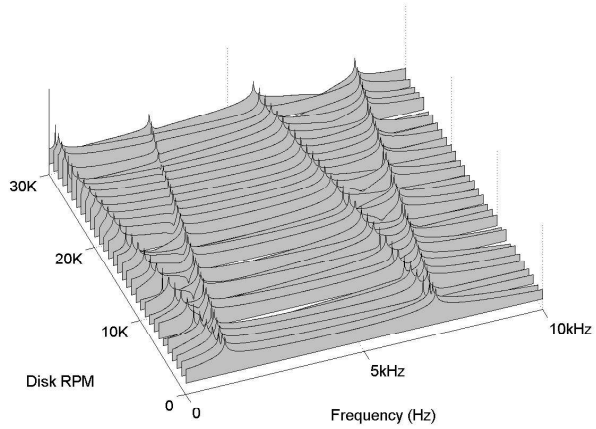

Figure 18: Waterfall plot showing the natural frequencies as a function of RPM. Modes (0,3) and (1,3)

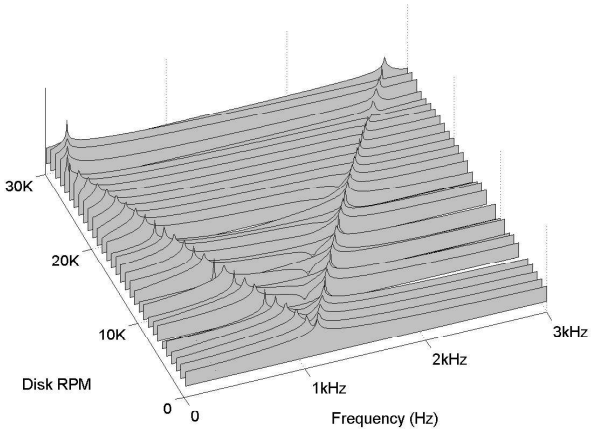

Figure 19: Closeup showing the critical behavior of mode $(0,3)_R$ at 27,000 RPM

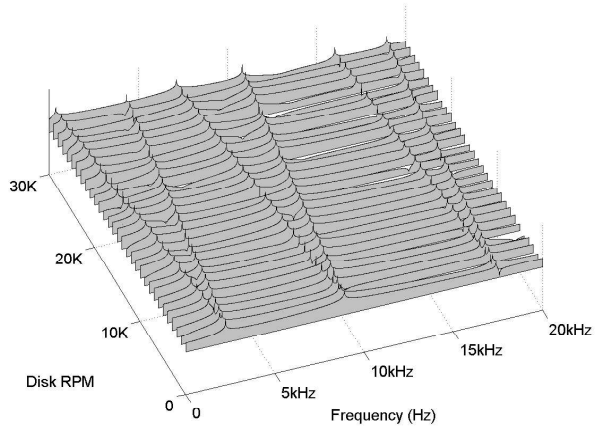

Figure 20: Waterfall plot showing the natural frequencies as a function of RPM. Modes (0,4), (1,4) and (2,4)

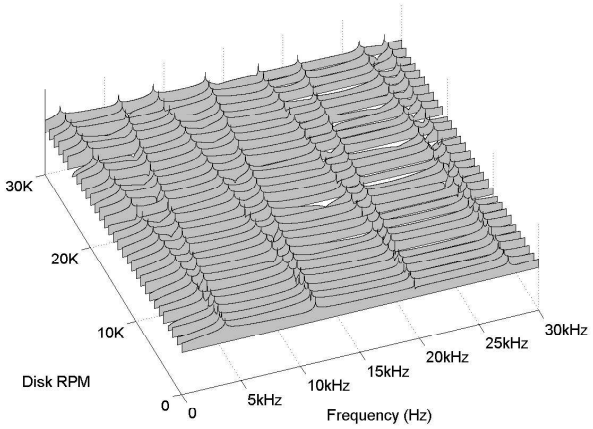

Figure 21: Waterfall plot showing the natural frequencies as a function of RPM. Modes (0,5), (1,5), (2,5) and (3,5)

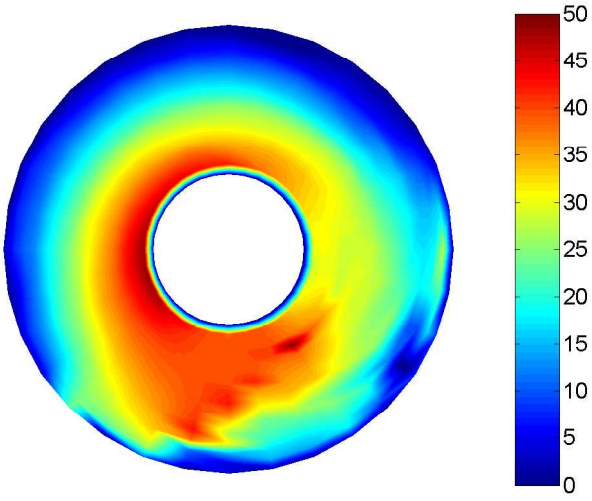

Figure 22: Mean resultant pressure distribution on the disk, for Case 1

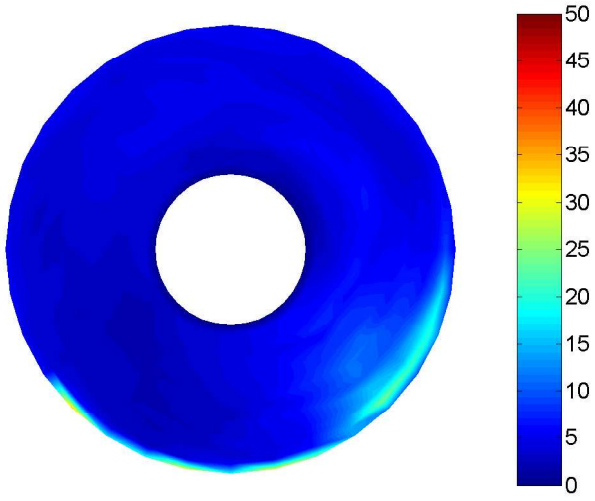

Figure 23: Mean resultant pressure distribution on the disk, for Case 2

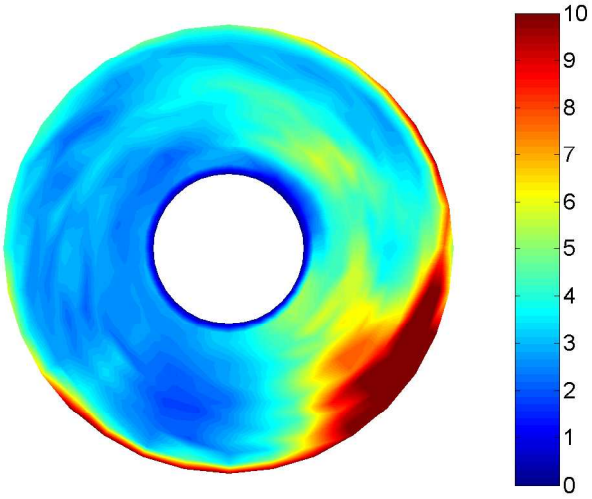

Figure 24: RMS resultant pressure distribution on the disk, for Case 1

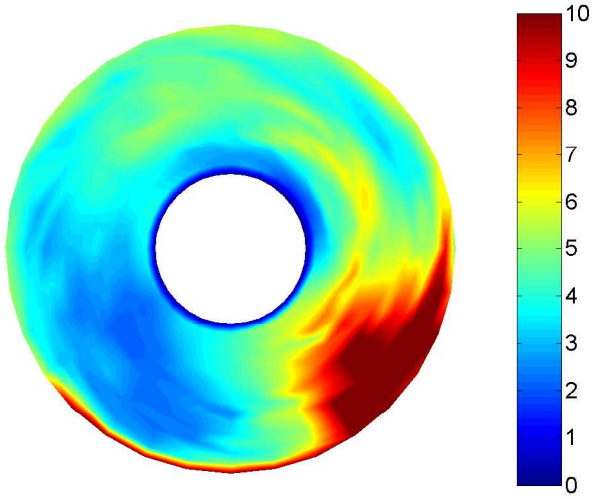

Figure 25: RMS resultant pressure distribution on the disk, for Case 2

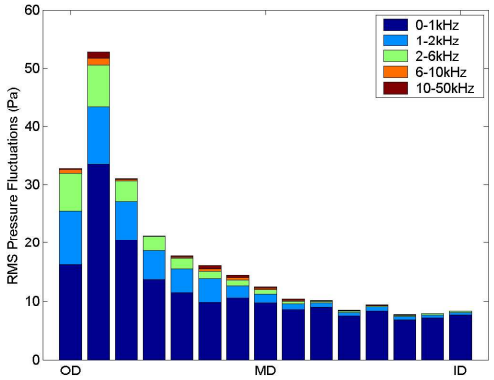

Figure 26: RMS Pressure fluctuations, broken down into contributions from frequency ranges. For Case 1 at 326 degrees.

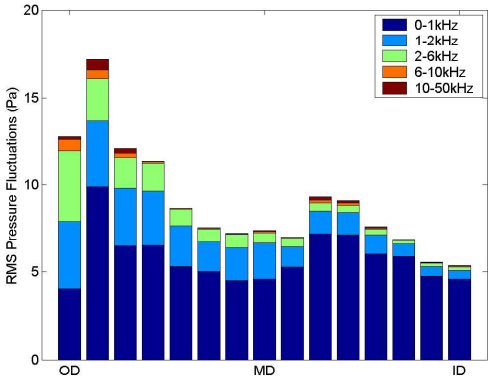

Figure 27: RMS Pressure fluctuations, for Case 1 at 0 degrees.

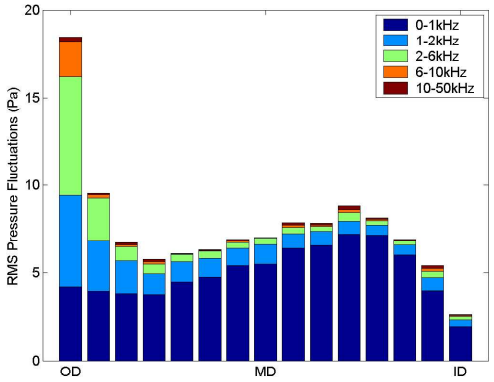

Figure 28: RMS Pressure fluctuations, for Case 1 at 56 degrees.

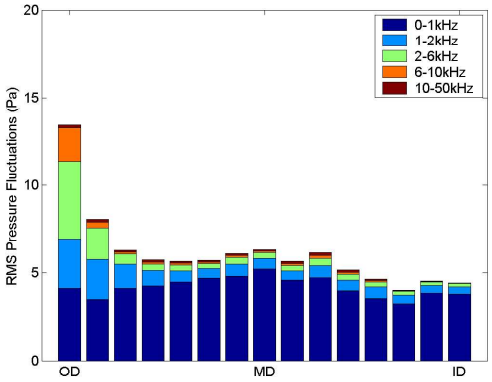

Figure 29: RMS Pressure fluctuations, for Case 1 at 112 degrees.

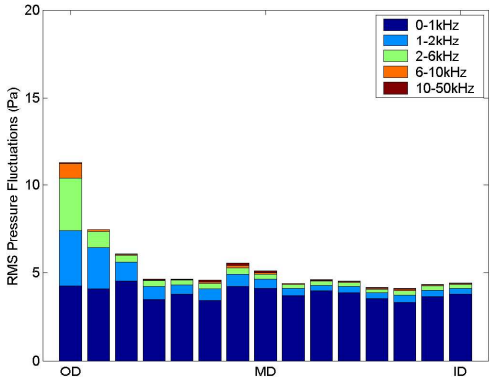

Figure 30: RMS Pressure fluctuations, for Case 1 at 180 degrees.

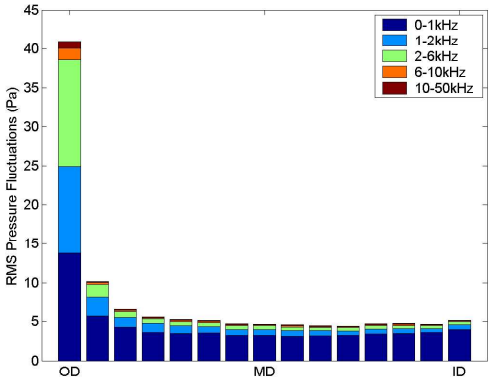

Figure 31: RMS Pressure fluctuations, for Case 1 at 236 degrees.

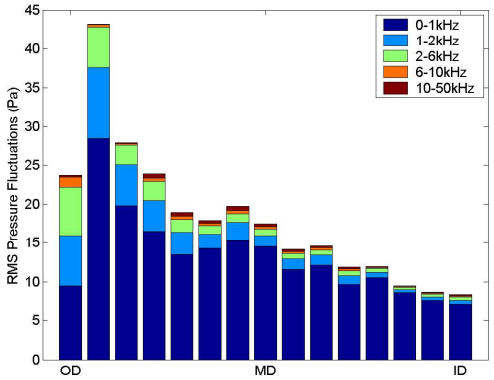

Figure 32: RMS Pressure fluctuations, broken down into contributions from frequency ranges. For Case 2 at 326 degrees.

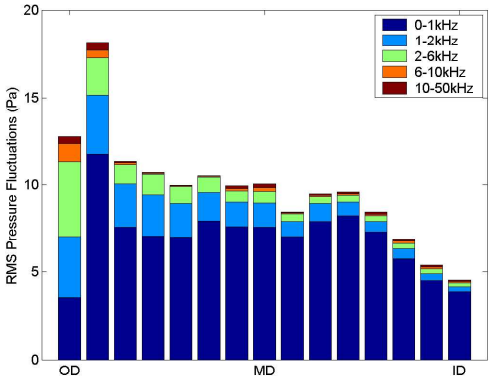

Figure 33: RMS Pressure fluctuations, for Case 2 at 0 degrees.

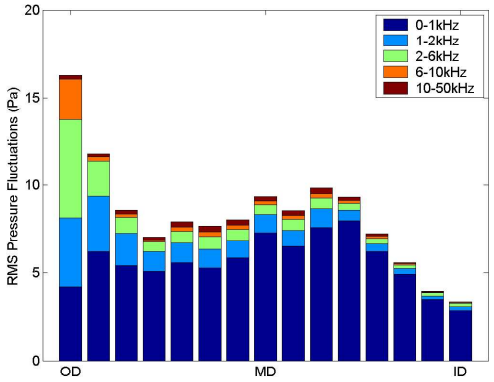

Figure 34: RMS Pressure fluctuations, for Case 2 at 56 degrees.

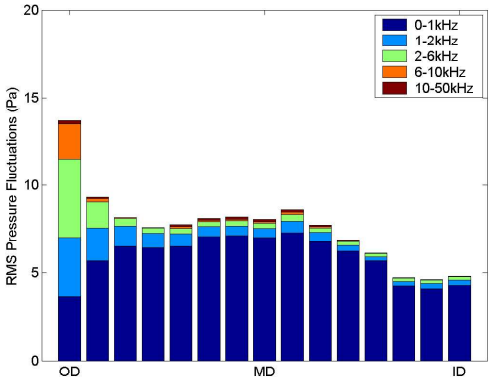

Figure 35: RMS Pressure fluctuations, for Case 2 at 112 degrees.

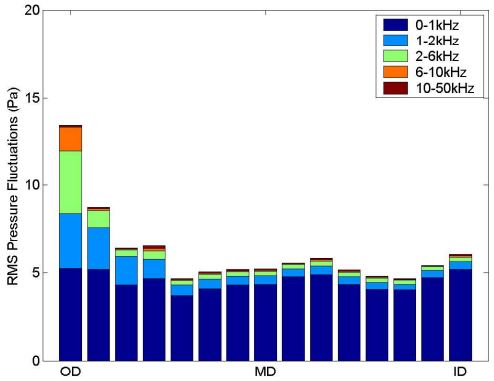

Figure 36: RMS Pressure fluctuations, for Case 2 at 180 degrees.

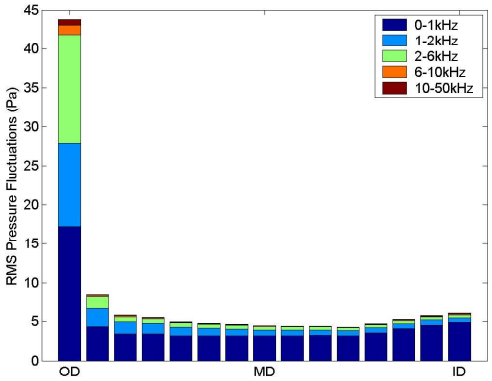

Figure 37: RMS Pressure fluctuations, for Case 2 at 236 degrees.

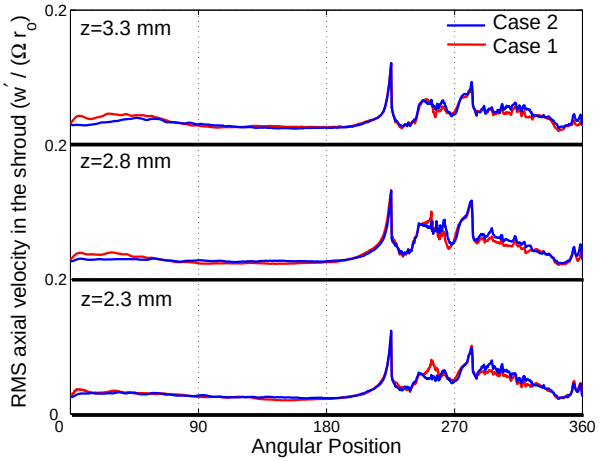

Figure 38: The RMS of the axial velocity at the center of the shroud gap, plotted for three different positions

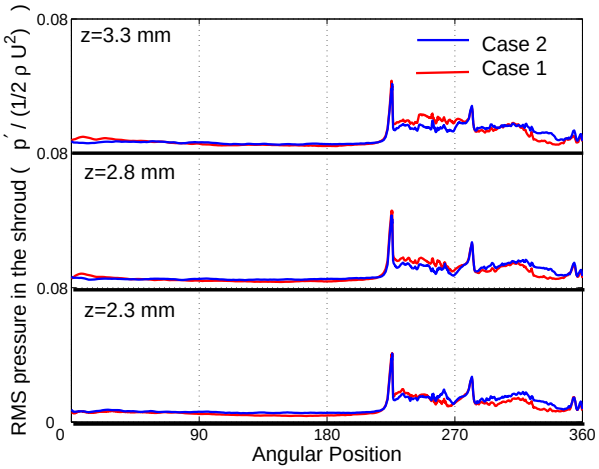

Figure 39: The RMS of the pressure fluctuations at the center of the shroud gap, plotted for three different positions

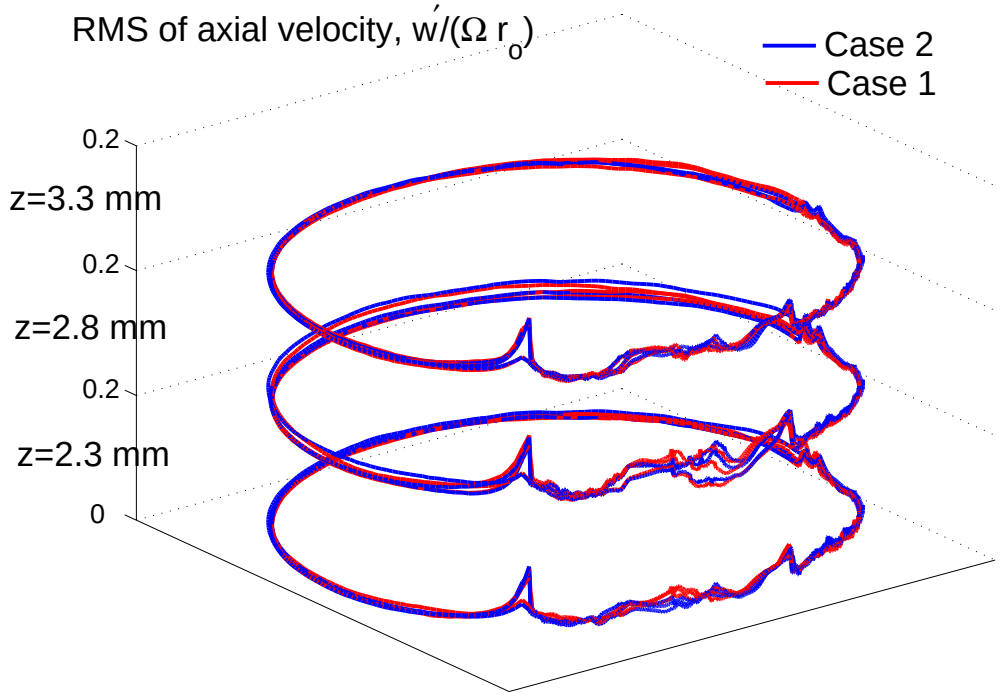

Figure 40: Three dimensional view showing the angular location of axial velocity fluctuations

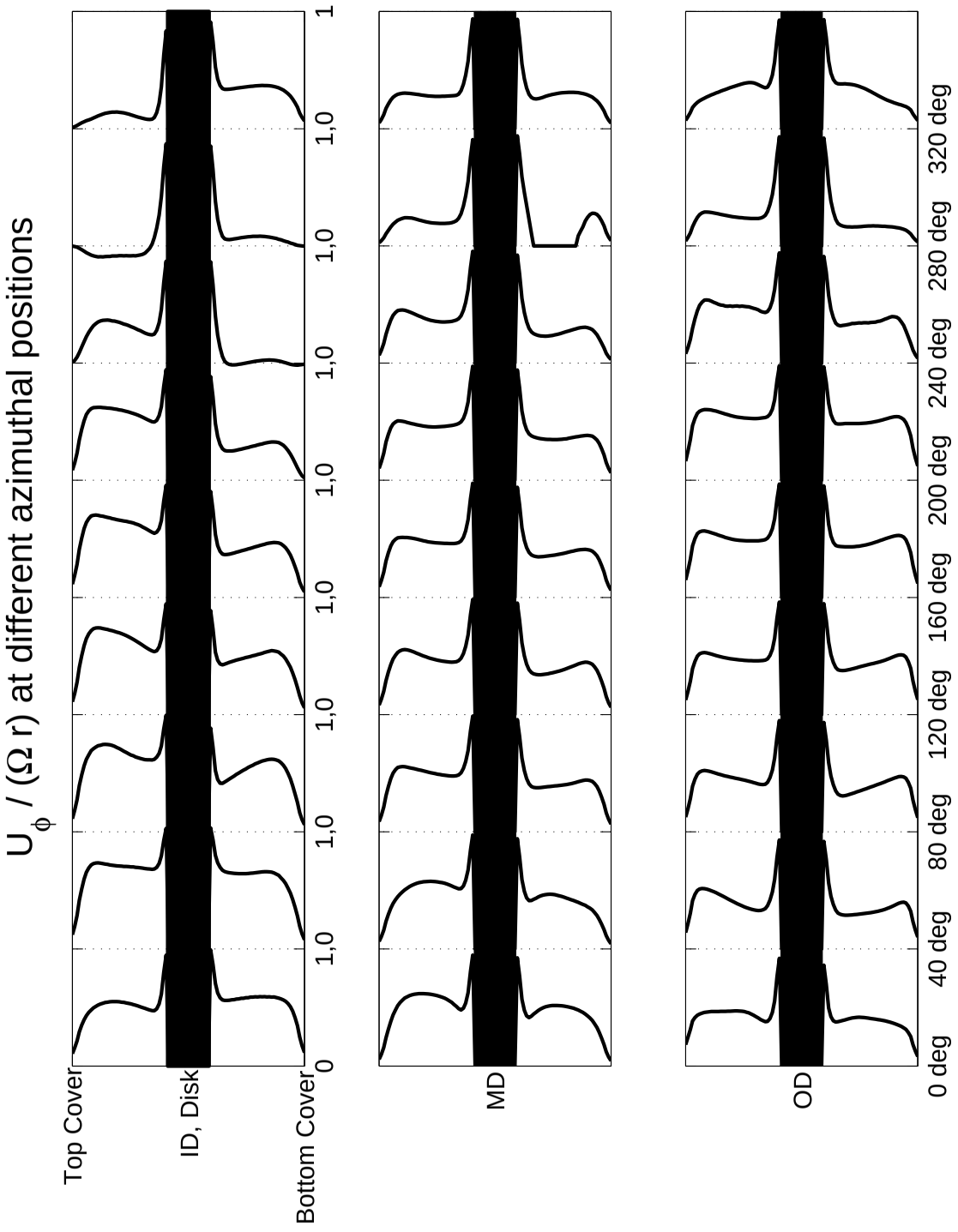

Figure 41: Interdisk non-dimensional velocity profile for Case 1, shown as a function of the azimuthal angle, for three positions, ID, MD and OD

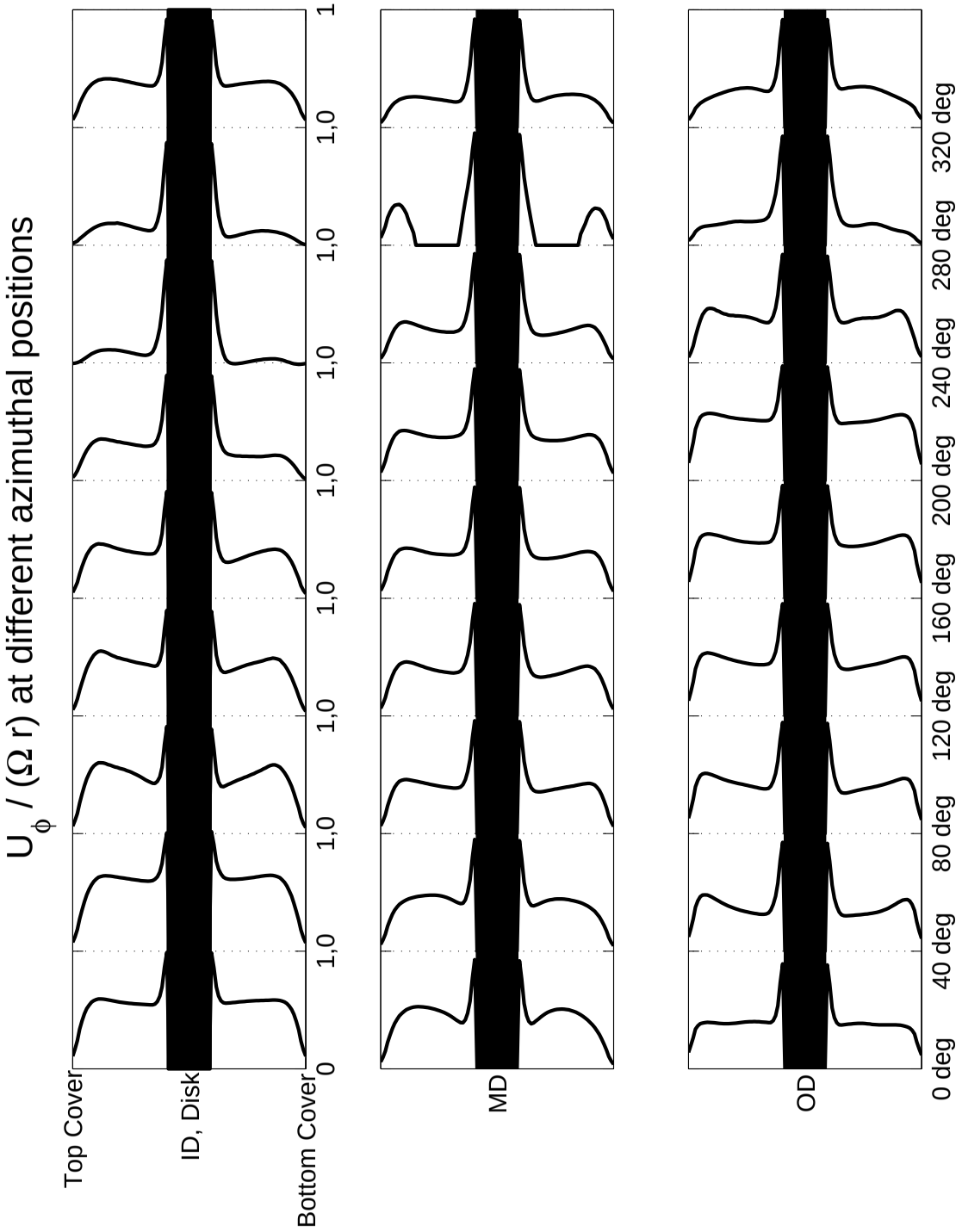

Figure 42: Interdisk non-dimensional velocity profiles for Case 2, shown as a function of the azimuthal angle, for three positions, ID, MD and OD

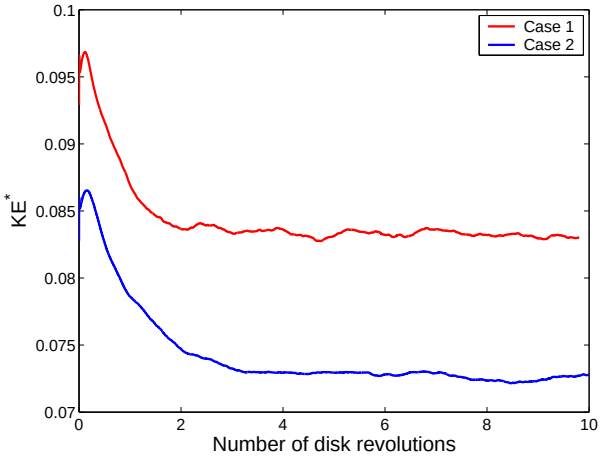

Figure 43: Non-dimensional kinetic energy

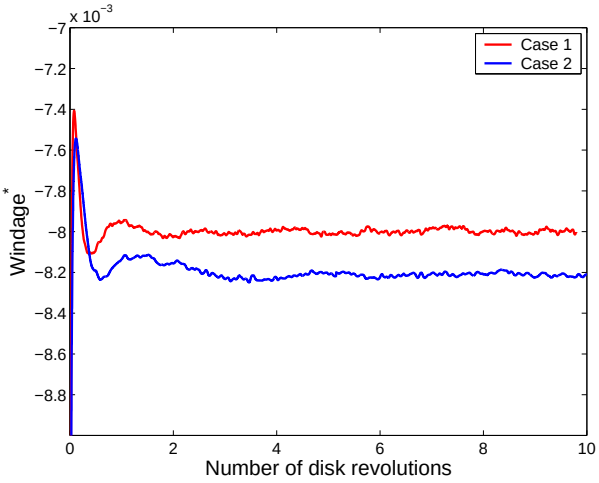

Figure 44: Non-dimensional windage

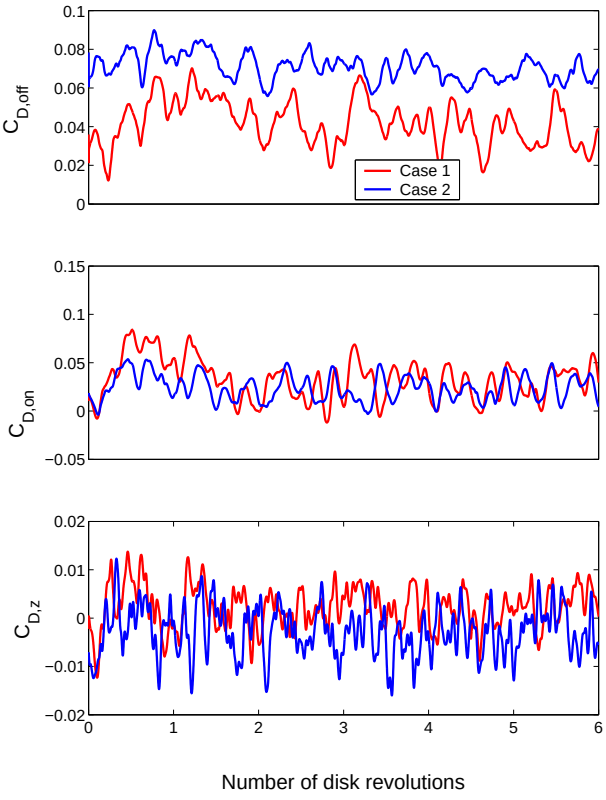

Figure 45: Time history of variation of coefficients of drag

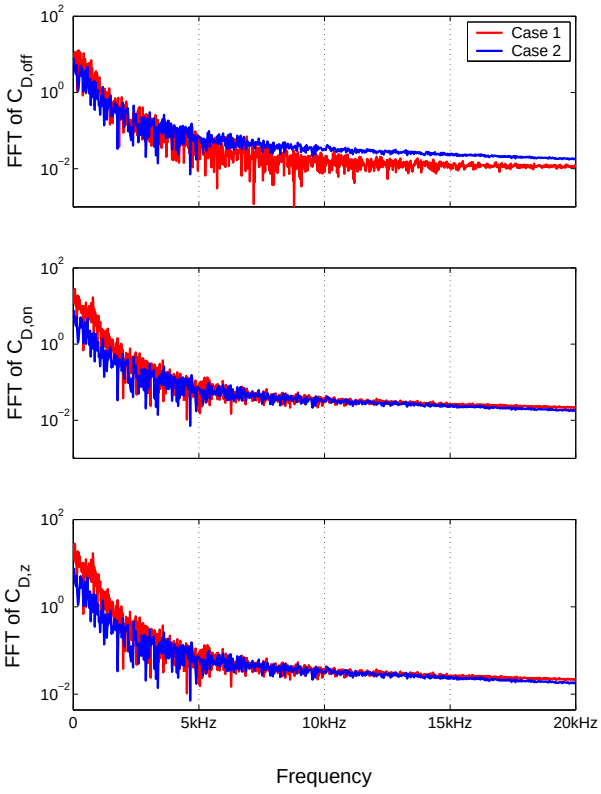

Figure 46: FFT of drag coefficients

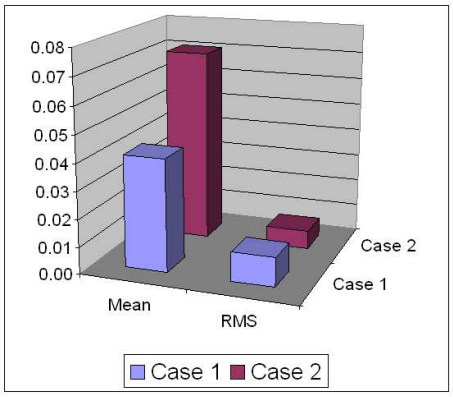

Figure 47: Summary of statistics for $C_{D,off}$

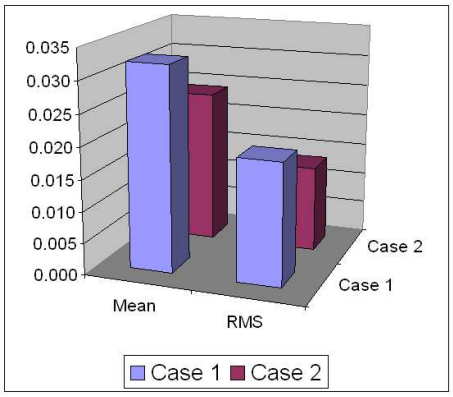

Figure 48: Summary of statistics for $C_{D,on}$

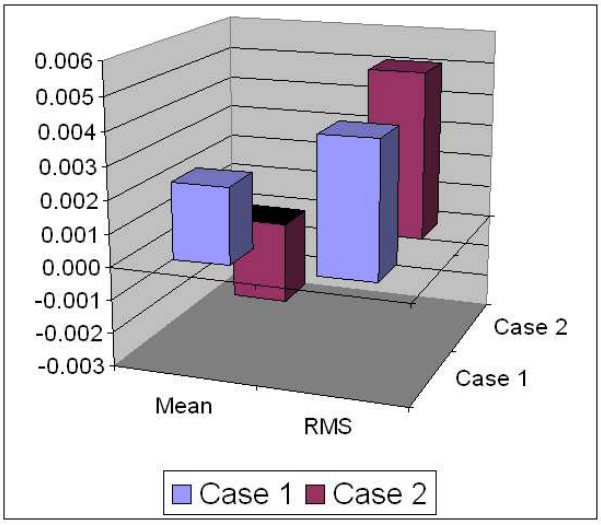

Figure 49: Summary of statistics for $C_{D,z}$

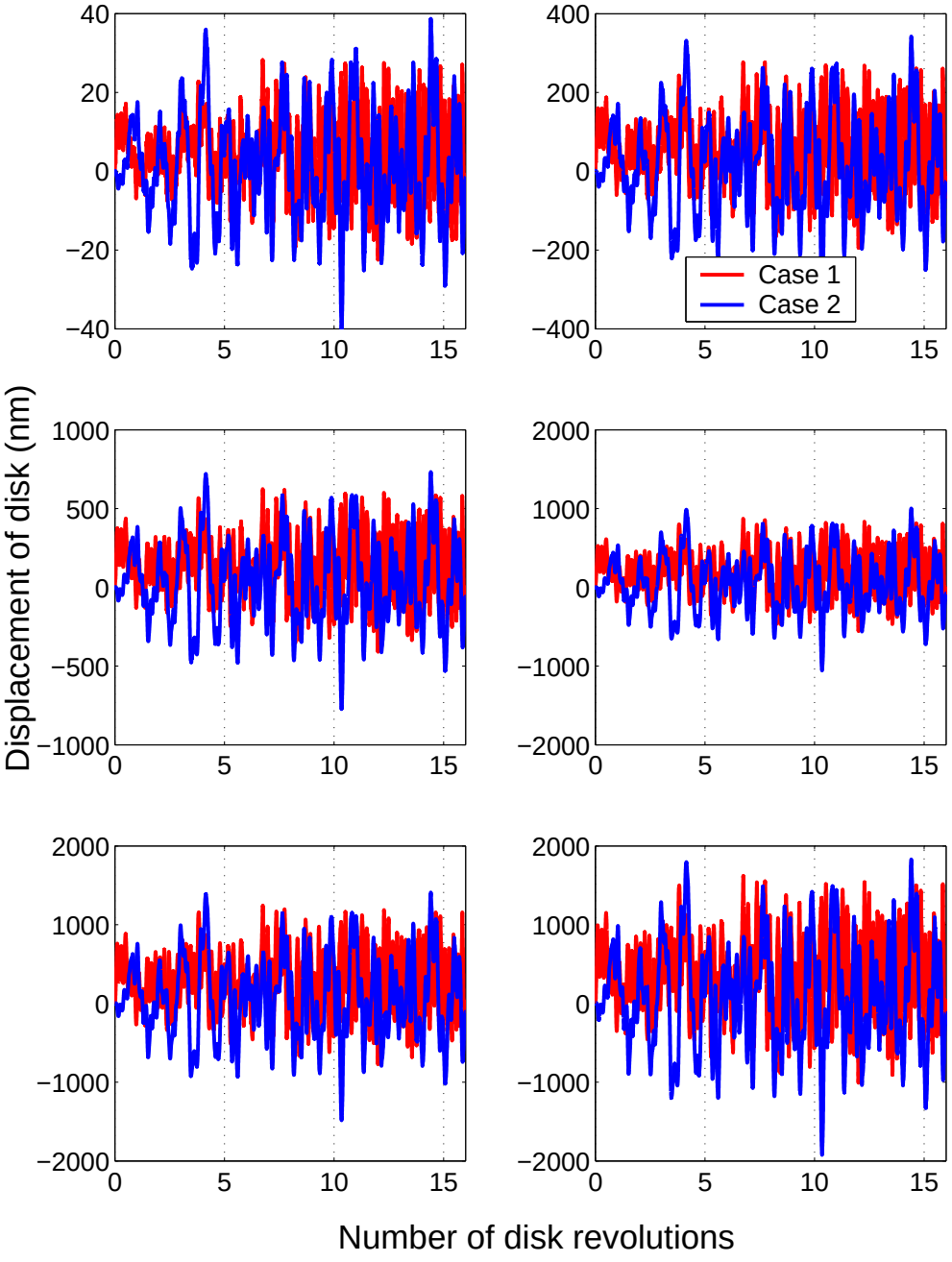

Figure 50: Disk vibration results showing the displacement of the disk as a function of time. Results are shown for points located at 12.5%, 31.25%, 50% (MD), 62.5 %, 81.25% and 100% (OD)

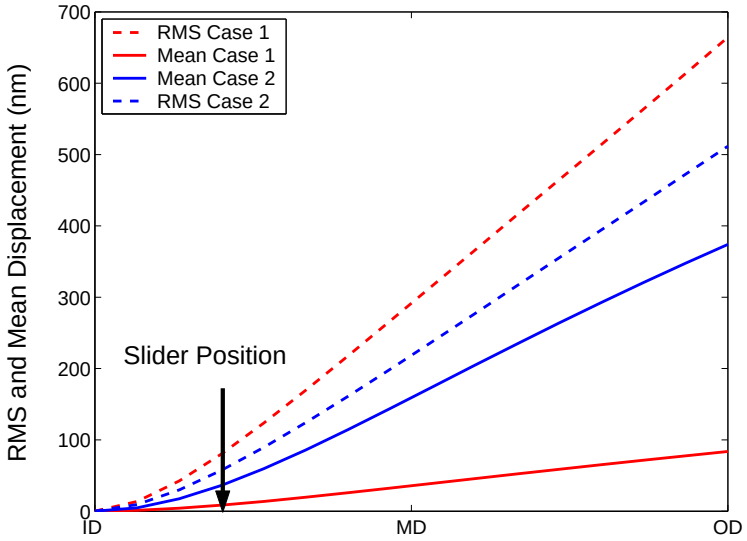

Figure 51: Summary of disk displacement results

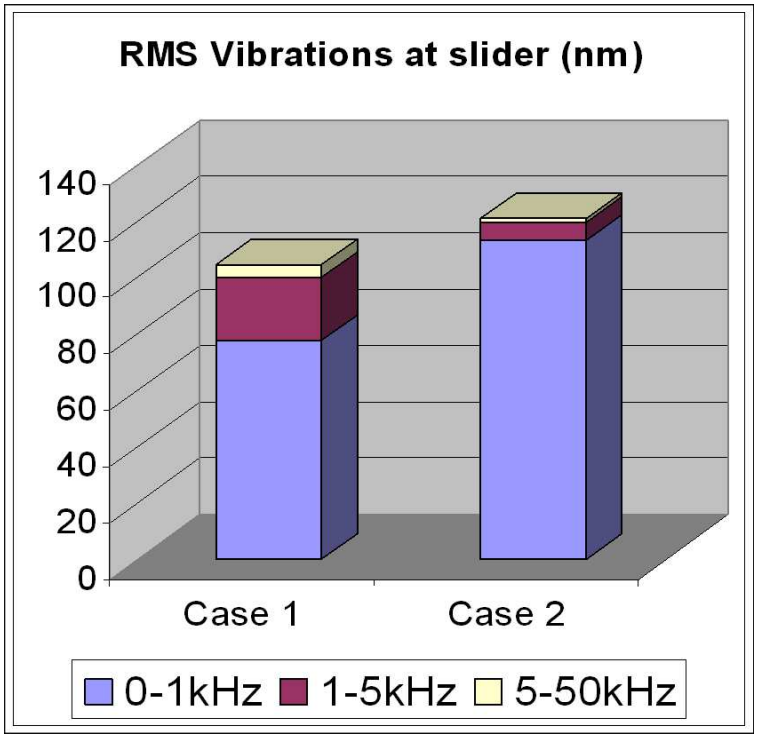

Figure 52: Contribution to the RMS disk vibrations under the slider from various frequency ranges